Supplementary information

Porous covalent organic nanotubes and their assembly in loops and toroids

In the format provided by the
authors and unedited

Supplementary Information

Porous covalent organic nanotubes and their assembly in loops and toroids

Kalipada Koner,[1,2] Shayan Karak,[1,2] Sharath Kandambeth,[3] Suvendu Karak,[3*] Neethu Thomas,[3] Luigi Leanza,[4] Claudio Perego,[5] Luca Pesce,[5] Riccardo Capelli,[4] Monika Moun,[6] Monika Bhakar,[6] Thalasseril G. Ajithkumar,[3] Giovanni M. Pavan,[4,5*] and Rahul Banerjee[1,2*]

[1]Department of Chemical Sciences, Indian Institute of Science Education and Research, Kolkata, Mohanpur, 741246, India.

[2]Centre for Advanced Functional Materials, Indian Institute of Science Education and Research, Kolkata, Mohanpur,741246, India.

[3]Central NMR Facility and Physical/Materials Chemistry Division, CSIR-National Chemical Laboratory, Dr. Homi Bhabha Road, Pune 411008, India

[4] Department of Applied Science and Technology, Politecnico di Torino, Torino 10129, Italy.

[5]Department of Innovative Technologies, University of Applied Sciences and Arts of Southern Switzerland, Viganello-Lugano CH-6962, Switzerland.

[6]Department of Physical Sciences, Indian Institute of Science Education and Research (IISER) Mohali, Sector 81, S. A. S. Nagar, Manauli, 140306, India.

Correspondence to *Email: r.banerjee@iiserkol.ac.in, suvkarak@gmail.com, giovanni.pavan@polito.it

Sr. No.	Contents	Page No.

General information

Materials:

For the synthesis of CONT-1, the starting materials *2,5*-dimethoxy*1,4*-benzenedicarbaldehyde (**DMDA**) and Tetraaminotriptycene (**TAT**) were synthesized following the previously reported literature protocols.[1,2] The commercially available Terephthalaldehyde (**TA**), *2*-methoxybenzaldehyde, and all solvents were purchased from Sigma-Aldrich and used without further purification.

Methods:

Fourier Transform Infrared (FT-IR): FT-IR spectra of the solid samples were recorded on a Bruker Optics ALPHA II spectrometer with a universal Zn-Se ATR (attenuated total reflection) accessory. All the data have been reported in the wavenumber (cm^{-1}) scale.

Nitrogen Adsorption Experiments (0 to 1 bar) were performed using Quantachrome Quadrasorb automatic and AutosorbiQ instrument. The nitrogen adsorption isotherms were collected at 77 K using a liquid nitrogen bath. Surface areas were calculated using the Brunauer-Emmett-Teller (BET) model applied between P/P_0 values of 0.05 and 0.3 for microporous and mesoporous CONTs. Corresponding pore size distributions were calculated using the non-localized density functional theory (NLDFT).

Activation of Sample for N_2 Adsorption Experiments: As synthesized, CONTs are separated from DCM by filtration. The resulting solid material was washed with excess DCM and Methanol. The solid was then dried overnight and degassed at 140 ℃ for 10 hours.

Thermogravimetric Analysis (TGA): TGA was carried out on a Mettler-Toledo TG50 and SDT Q600 TG-DTA analyzer under N_2 atmosphere from 30 °C to 900 °C along with a ramp rate of 10°C min^{-1}. Before carrying out the TGA, the samples were activated at 100 °C for 30 minutes to eliminate the samples' water.

Scanning Electron Microscopy (SEM): SEM images were obtained using Zeiss DSM 950 and FEI QUANTA200 3D microscope operating at 10 kV using tungsten filament as the electron source. Before the imaging, the samples were sputtered with gold (nano-sized film) using an SCD 040 Balzers Union sputterer to avoid charging during SEM analyses. The samples were prepared simply by putting a drop of dispersed samples in DCM or *o*-Xylene or THF on a clean piece of Silicon wafer.

Transmission Electron Microscopy (TEM): TEM images were obtained using FEI Tecnai G2 F20 X-TWIN TEM at an accelerating voltage of 200 kV. The samples were prepared by direct drop-casting onto copper grids TEM Window (TED PELLA, INC. 200 mesh).

Dynamic Light Scattering (DLS): DLS experiments were performed using Litesizer™ 500 equipped with a 658 nm, 40 mW laser at 20 °C with 10 mm pathlength quartz cuvette. The data was analyzed using Kalliope™ software.

Solid-State NMR (SSNMR) Instrument Details: All ^{13}C and ^{15}N NMR spectra were recorded on a Bruker AV NEO 500-MHz instrument (magnetic field =11.7 T, Larmor frequency of ^{13}C =125.7MHz, ^{15}N=50.697).
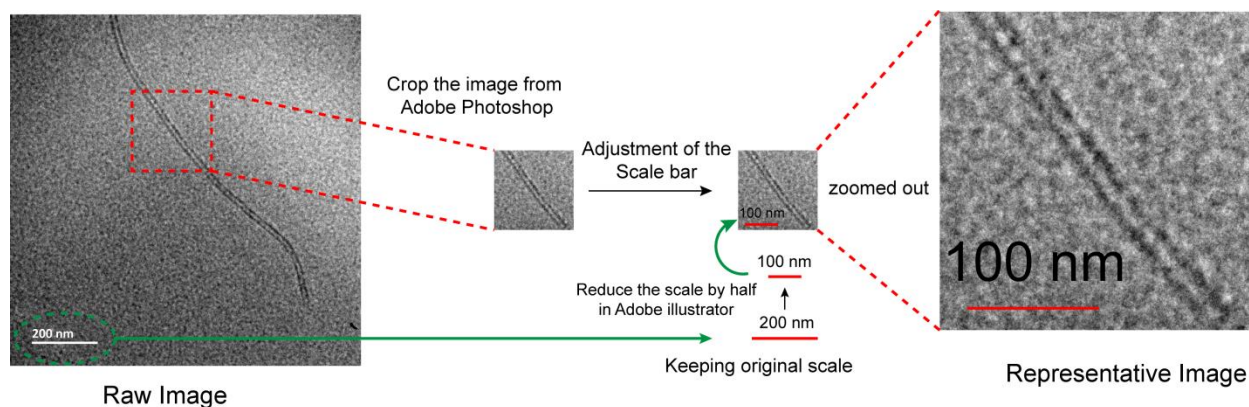
^{13}C SSNMR Experiments: For both CP-MAS and HPDEC experiments, Bruker PH MAS DVT 500W2 BL 4 N-P/F/H probe equipped with 4 mm zirconia rotor was used at a spinning frequency of 14.5 kHz. The frequency scale in ppm was referenced to adamantine C-H peak. ^{13}C CP MAS NMR spectra were recorded with a contact time of 5 ms, and a 2 s and 3 s recycle delay for Batch 1 and 2, respectively. The number of averages was 16000. ^{13}C high-power proton decoupling (HPDEC) MAS experiment was performed to obtain ^{13}C quantitative spectrum since it non-selectively excites all nuclei, unlike CP-MAS. ^{13}C T1relaxation time was calculated using the method of Torchia. HPDEC spectra were recorded after excitation with a $\pi/2$ pulse of 3.725 µs with a recycling delay of 1000 s. 256 transients were accumulated for a spectrum for batch 1 and 2. For batch 3, JEOL JNM ECX 400 MHz instruments (magnetic field =9.39798T, Larmor frequency of 13C =100.613MHz) in 4mm Double resonance probe NM-03081CPM4 (SH40T4) with a spinning frequency of 14 kHz is used. The number of scans for the batch 3 sample is 1231.

^{15}N CPMAS: ^{15}N CPMAS experiments were performed in Bruker PH MAS DVT 500W2 BL 4 N-P/F/H probe and 4mm zirconium rotor. The spinning frequency was 14.5 kHz. The spectra were obtained at a ^{1}H-^{15}N CP contact time of 3.5 ms and a pulse repetition delay of 2 s. The chemical shifts are reported relative to NH4Cl.
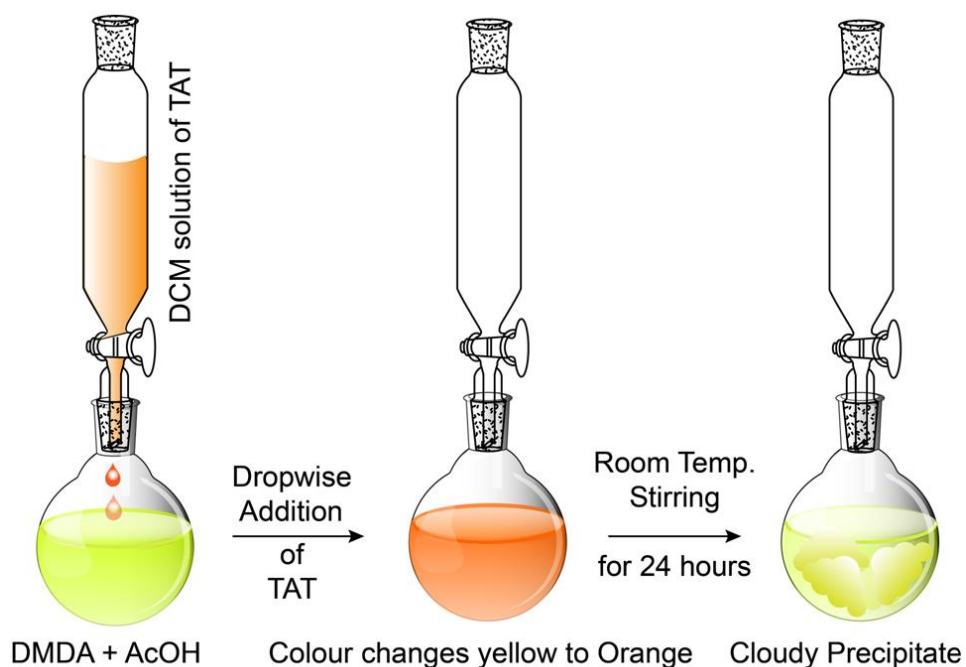
Atomic Force Microscopy on Polymer Nanotubes/Si Sample: The samples (polymer nanotubes/Si) was mounted on the sample stage of an atomic Force Microscope (MFP 3D of Asylum Research), and morphology of the sample was obtained. Atomic force microscopy measurements were performed in non-contact mode using Si cantilevers with Pt-Ir coating in ambient conditions. The resonance frequency of AFM probes was around 320 kHz. In the topography, single, entangled, and circular nanotubes were observed.

Model of CONTs: The model structure was developed by both geometry and energy optimisation in "Material Studio" software.

Processing of SEM and TEM Images: The raw files of both SEM and TEM images are processed in the following sequence to maintain the scale bar and aspect ratio intact.

Crop the image from Adobe Photoshop

Adjustment of the Scale bar

zoomed out

100 nm

Reduce the scale by half in Adobe illustrator

100 nm

200 nm

Keeping original scale

100 nm

Raw Image

Representative Image

Section 1: Synthetic Procedures

Supplementary Figure 1: The detailed synthetic procedure of both CONT-1 and CONT-2 synthesis. The colors are well accordance with the actual color changes.

General Synthetic Procedure:

Synthesis of CONT-1. *2,5*-dimethoxy-*1,4*-benzene dicarbaldehyde (DMDA) (19.4 mg, 0.1 mmol) was dissolved in 100 mL CH_2Cl_2 (dry, O_2-free), and 0.5 mL 6 (M) AcOH was added directly into the yellow-colored homogeneous solution as a catalyst of Schiff base reaction. A solution of tetraaminotryptycene (TAT) (15.7 mg, 0.05 mmol) in 50 mL CH_2Cl_2 (dry, O_2-free) was added dropwise using a dropping funnel with stirring at room temperature under argon atmosphere for 24 hours. The resulting cloudy precipitate was filtered and washed with excess anhydrous methanol. Yield: 25 mg ,78% (calculated with respect to TAT).

Synthesis of CONT-2. Terephthalaldehyde (TA) (13.4 mg, 0.1 mmol) was dissolved in 100 mL dry degassed Dichloromethane (DCM), and 0.5 mL 6 (M) AcOH was added directly into solution as a catalyst of Schiff base reaction. A solution of tetraaminotryptycene (TAT) (15.7 mg, 0.05 mmol) in 50 mL dry DCM was added dropwise using a dropping funnel with stirring at room temperature under Argon atmosphere for 24 hours. The resulting cloudy precipitate was filtered and washed with excess anhydrous methanol. Yield: 13.3 mg, 51% (calculated with respect to TAT).

Section 2: Monomer Synthesis

In the typical monomer synthesis, *2*-methoxybenzaldehyde (27.2 mg, 0.2 mmol) was taken in dry DCM in the presence of 6 (M) AcOH as the catalyst. Dilute DCM solution of TAT (15.7 mg, 0.05 mmol) was then added to the reaction mixture and stirred for 24 hours. The dry yellow powder was collected after the evaporation of DCM. The powder was dissolved in methanol and characterized by High-Resolution Mass Spectroscopy (HRMS).
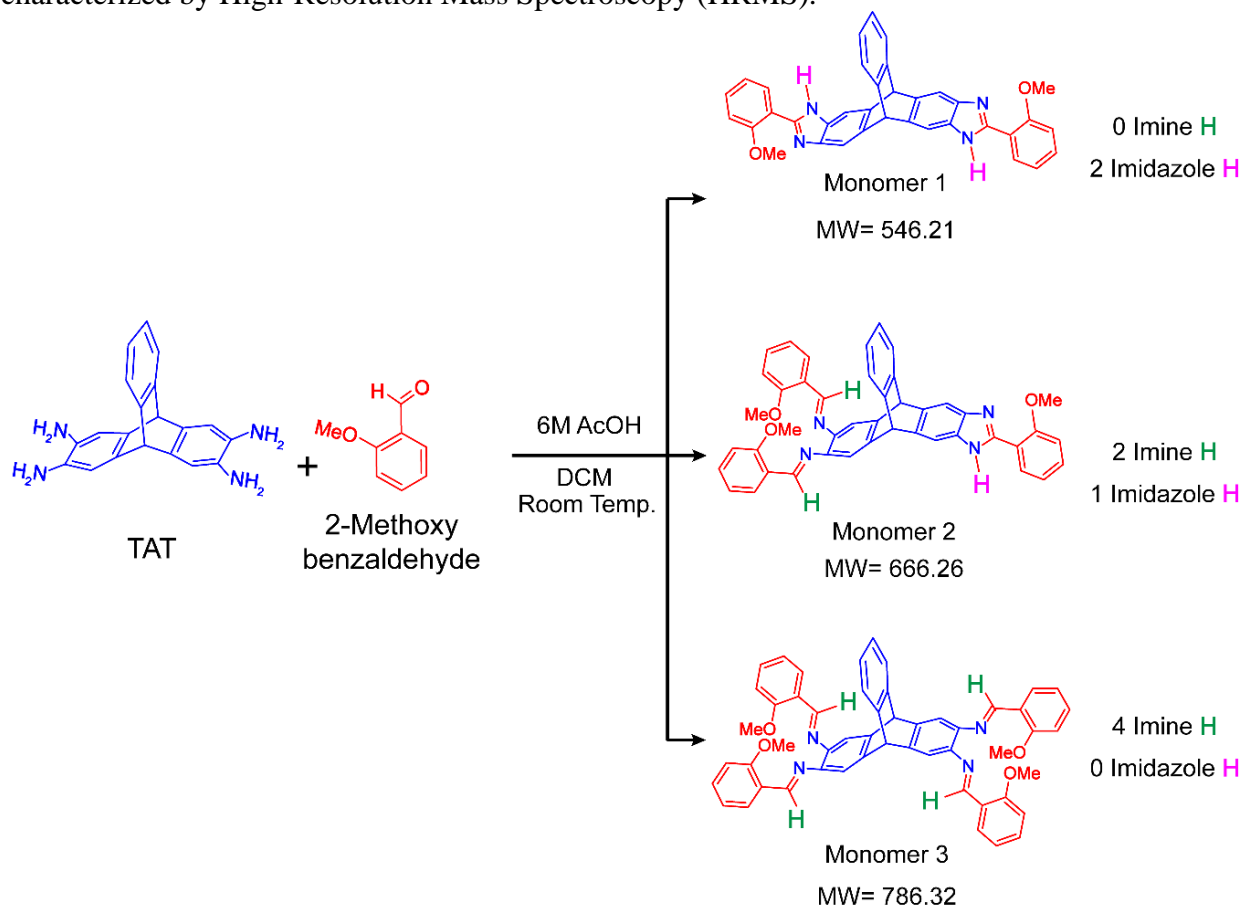
Supplementary Figure 2: Monomers formed in the reaction of TAT and 2-methoxy benzaldehyde.

HRMS analysis indicates that the stoichiometric condensation of TAT and *2*-methoxybenzaldehyde results in a mixture of three compounds Monomer 1 [m/z ($C_{36}H_{26}N_4O_2$) = 547.22 (M+H)$^+$], Monomer 2 [m/z ($C_{44}H_{34}N_4O_3$)= 667.28 (M+H)$^+$], and Monomer 3 [m/z ($C_{52}H_{42}N_4O_4$)= 787.34 (M+H)$^+$]. Out of those, only the bonding pattern in monomer 3 will eventually lead to the nanotubular architecture as the final product when we replace monoaldehyde with dialdehyde**.** However, monomer 2 will also lead to nanotube formation but with a considerable amount of defect centers.

6

Table 1: *Detail information of all the conditions used for the optimization of Imine bonding over imidazole ring formation.*[a]

| Condition	Solvent	Catalyst	Temperature	Atmosphere	Dilution (mL)	Ratio from ¹H NMR Studies		Ratio from HRMS Studies		
						Imine H	Imidazole H	Monomer 1	Monomer 2	Monomer 3
1	Ethanol	1M AcOH	Reflux	Open	50	0	1	1	0	0
2	Methanol	1M AcOH	Reflux	Open	50	0.36	1	0.13	1	0.39
3	DCM	1M AcOH	Reflux	Open	50	0.74	1	0.08	1	0.11
4	DCM	1M AcOH	Reflux	Argon	50	1	0.79	0.85	0.62	1
5	DCM	3M AcOH	Reflux	Argon	50	1	0.45	0.23	1	0.40
6	DCM	6M AcOH	Reflux	Argon	50	1	0.31	0.02	0.47	1
7	DCM	HCl	Reflux	Argon	50	1	0.21	0.02	0.28	1
8	DCM	TFA	Reflux	Argon	50	1	0.13	0.08	0.22	1
9	DCM	AcOH	Reflux	Argon	50	1	0.11	0.04	0.17	1
10	DCM	6M AcOH	Room Temp	Argon	50	1	0.05	0.01	0.12	1
11	DCM	6M AcOH	Room Temp	Argon	100	1	0.01	0.01	0.08	1
12	**DCM**	**6M AcOH**	**Room Temp**	**Argon**	**200 mL**	**1**	**0**	**0**	**0**	**1**

[a] 0.2 mmol of 2-methoxybenzaldehyde and 0.05 mmol of tetraaminotryptycene (TAT) are used for monomer synthesis

The optimized condition has been used to reduce the yield of the side products particularly. The sequential modifications of the synthetic conditions for the model monomeric compound lead to achieving the optimized condition where the yield of the desired compound is 100% [Supplementary Table 1].

From NMR studies, we have calculated the ratio of imine and imidazole bonding present in the reaction mixture (Supplementary Figure 3-8). As monomer 2 contains both imine and imidazole bonding from NMR, it is difficult to calculate the ratio of three monomers. However, to calculate the ratio of three monomers, we have performed High-Resolution Mass Spectroscopy (HRMS) (Supplementary Figure 3-8). The condition (Condition 12) for monomer 3 formation is optimized from both NMR and HRMS studies.
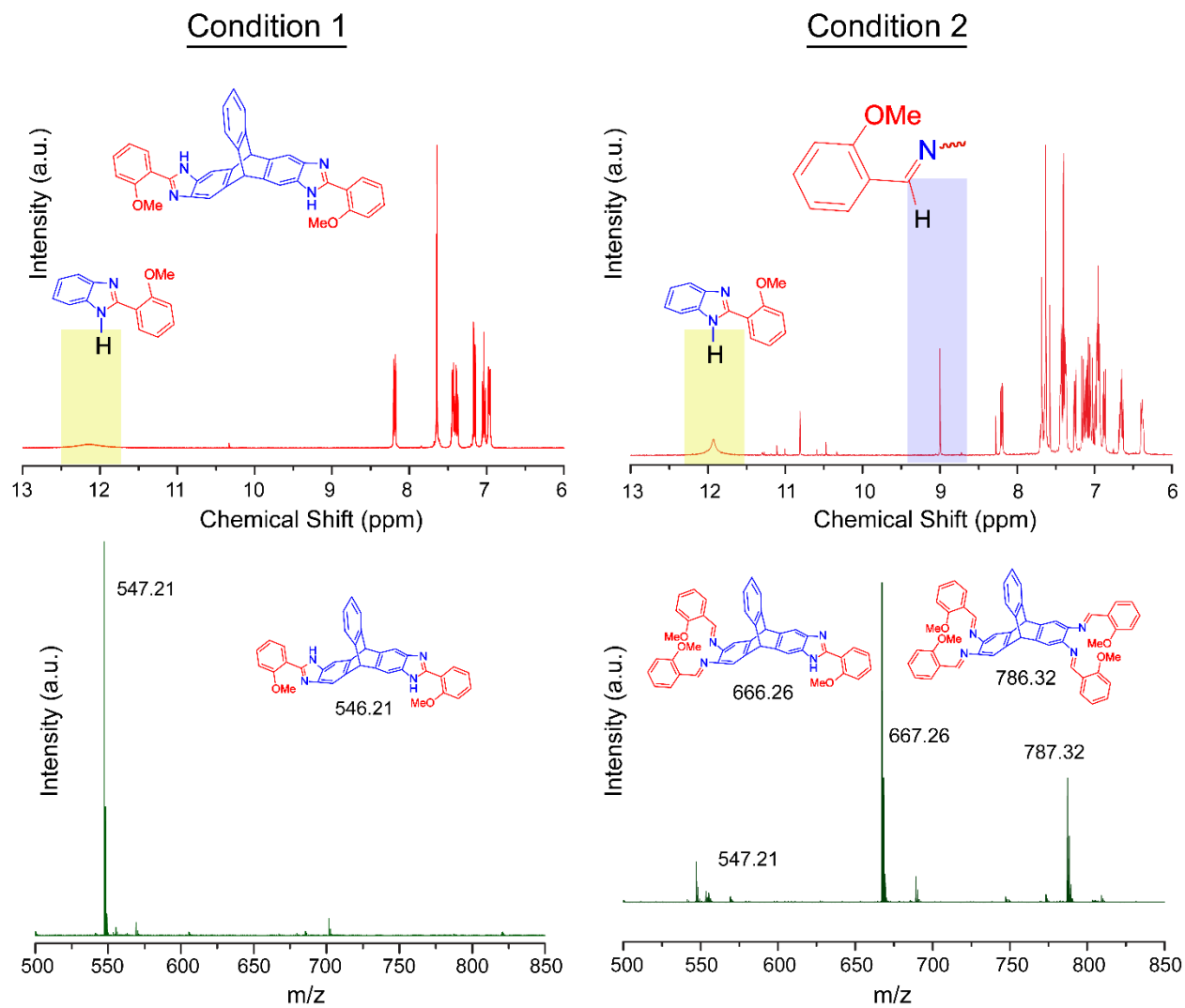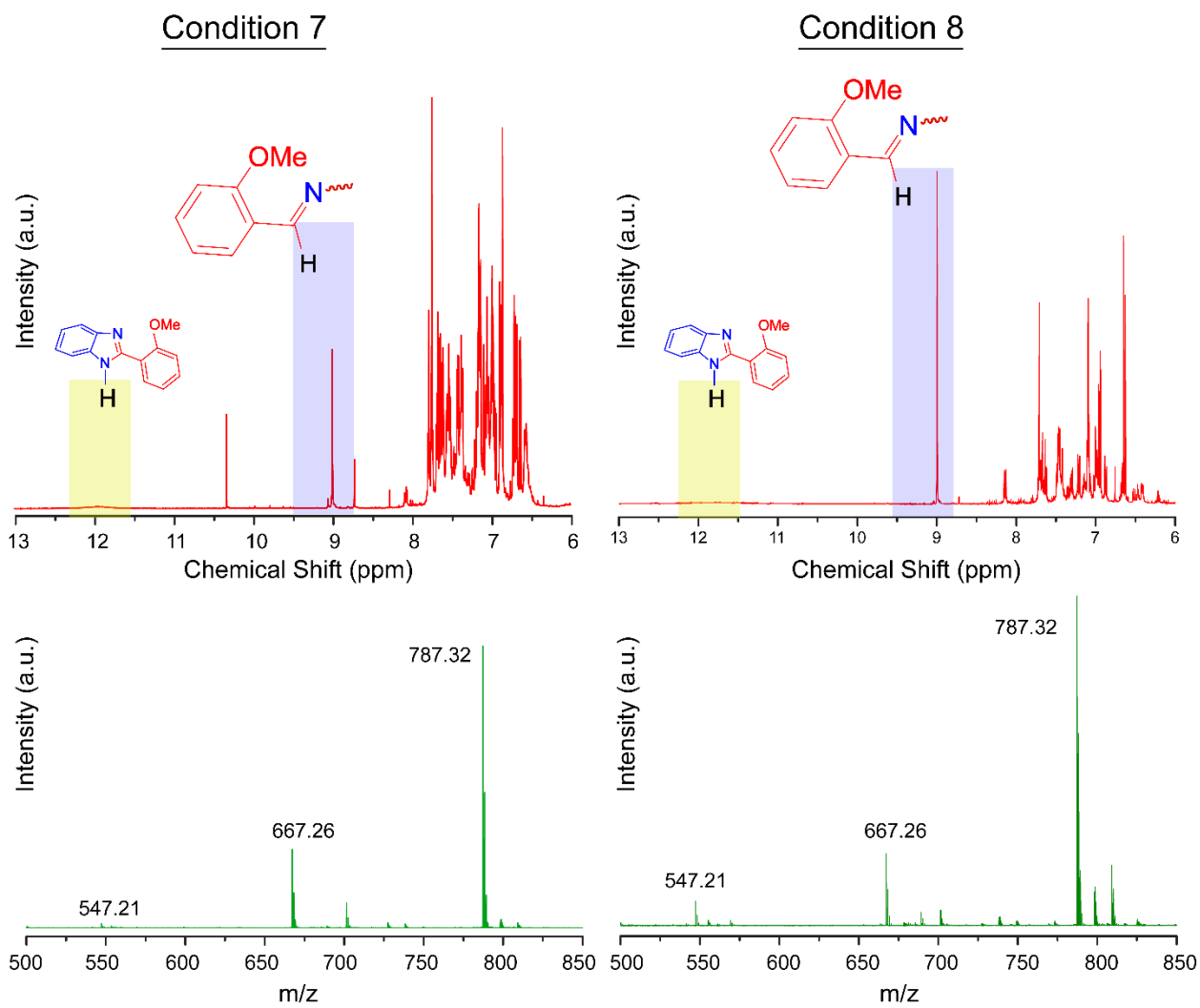
Supplementary Figure 3: Calculation of ratio between Imine and Imidazole bonding from 1H NMR studies (Red) and the ratio between three monomers from HRMS data (Green) of the reaction crude at conditions 1 and 2.
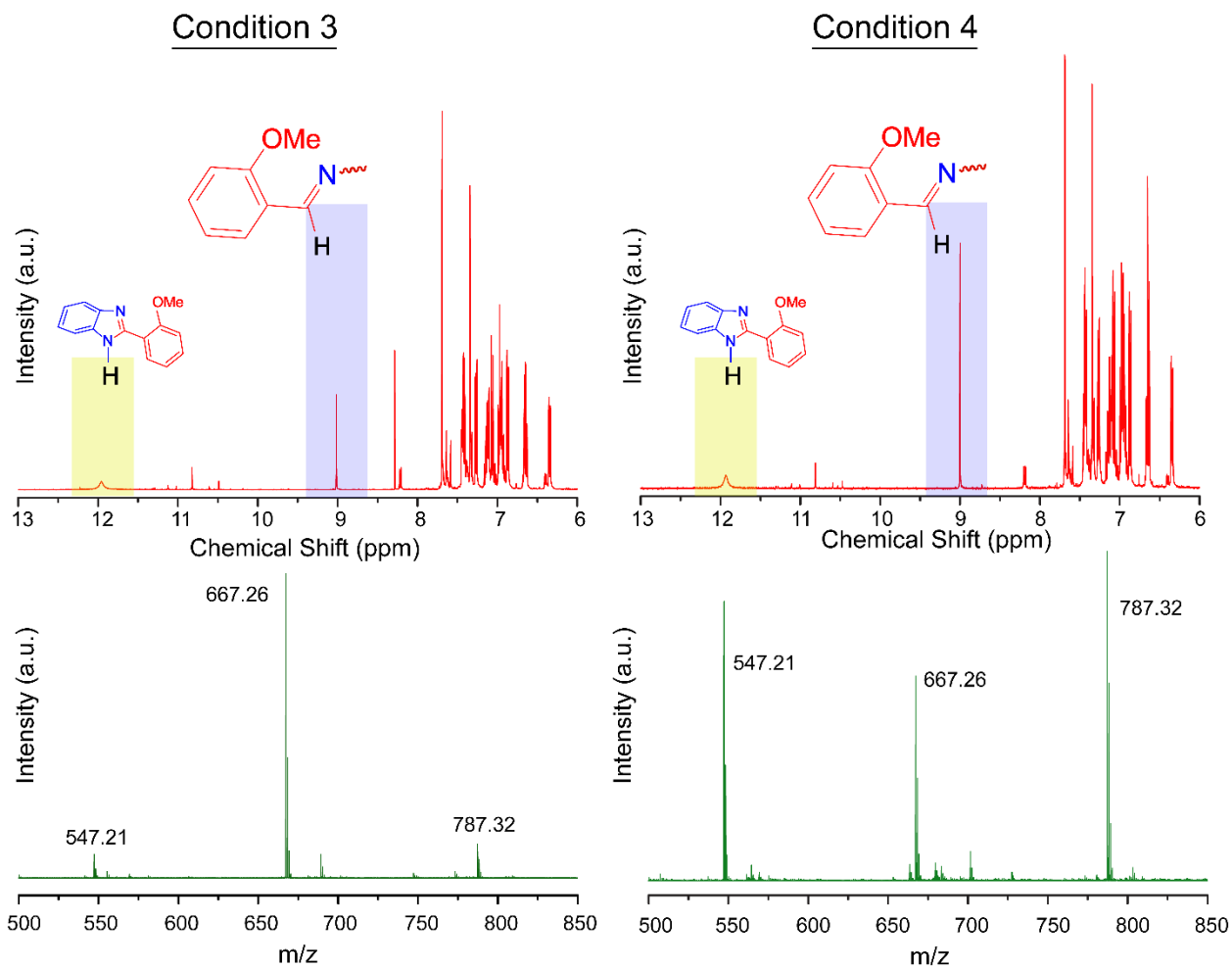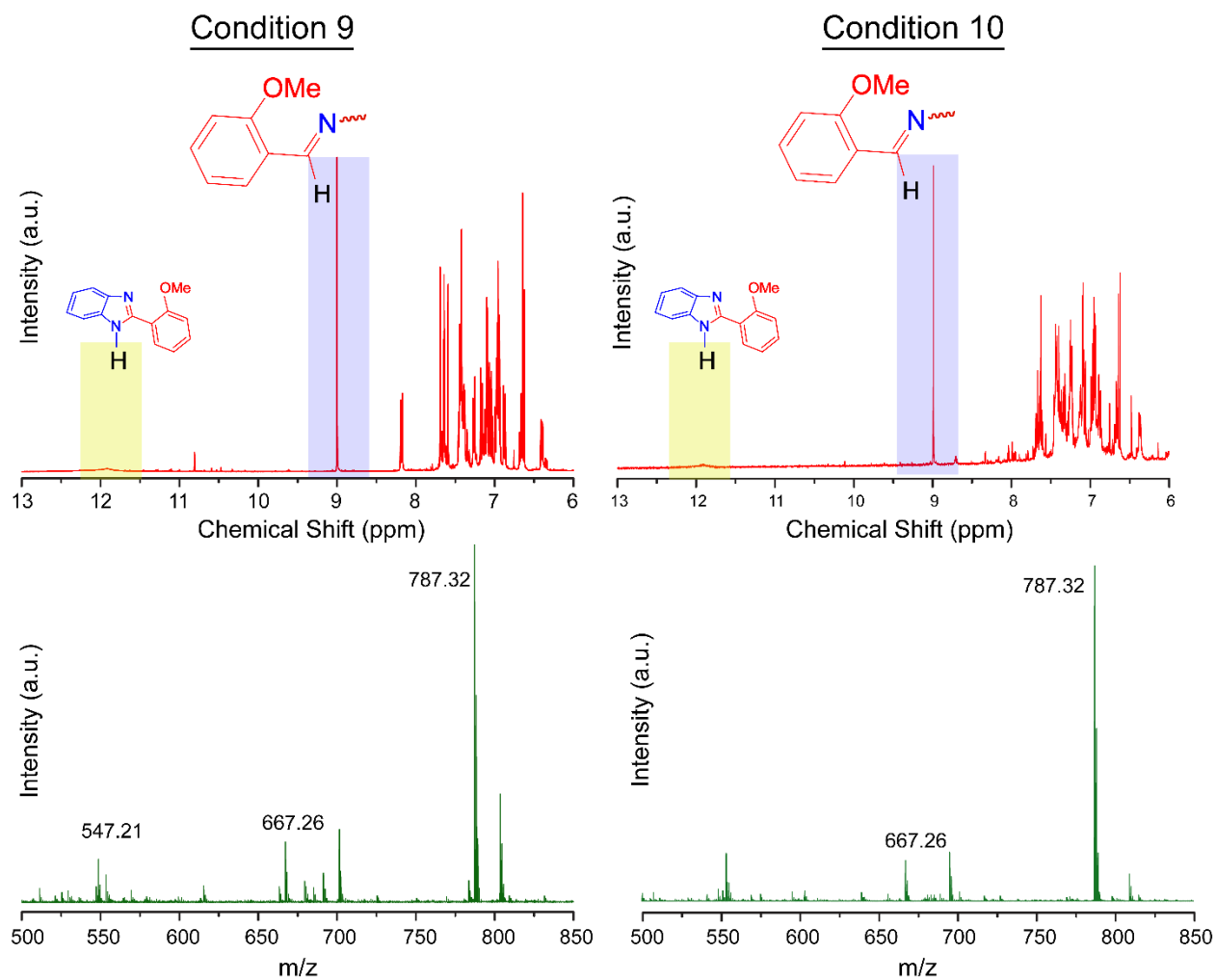
Supplementary Figure 4: Calculation of ratio between Imine and Imidazole bonding from 1H NMR studies (Red) and the ratio between three monomers from HRMS data (Green) of the reaction crude at conditions 3 and 4.
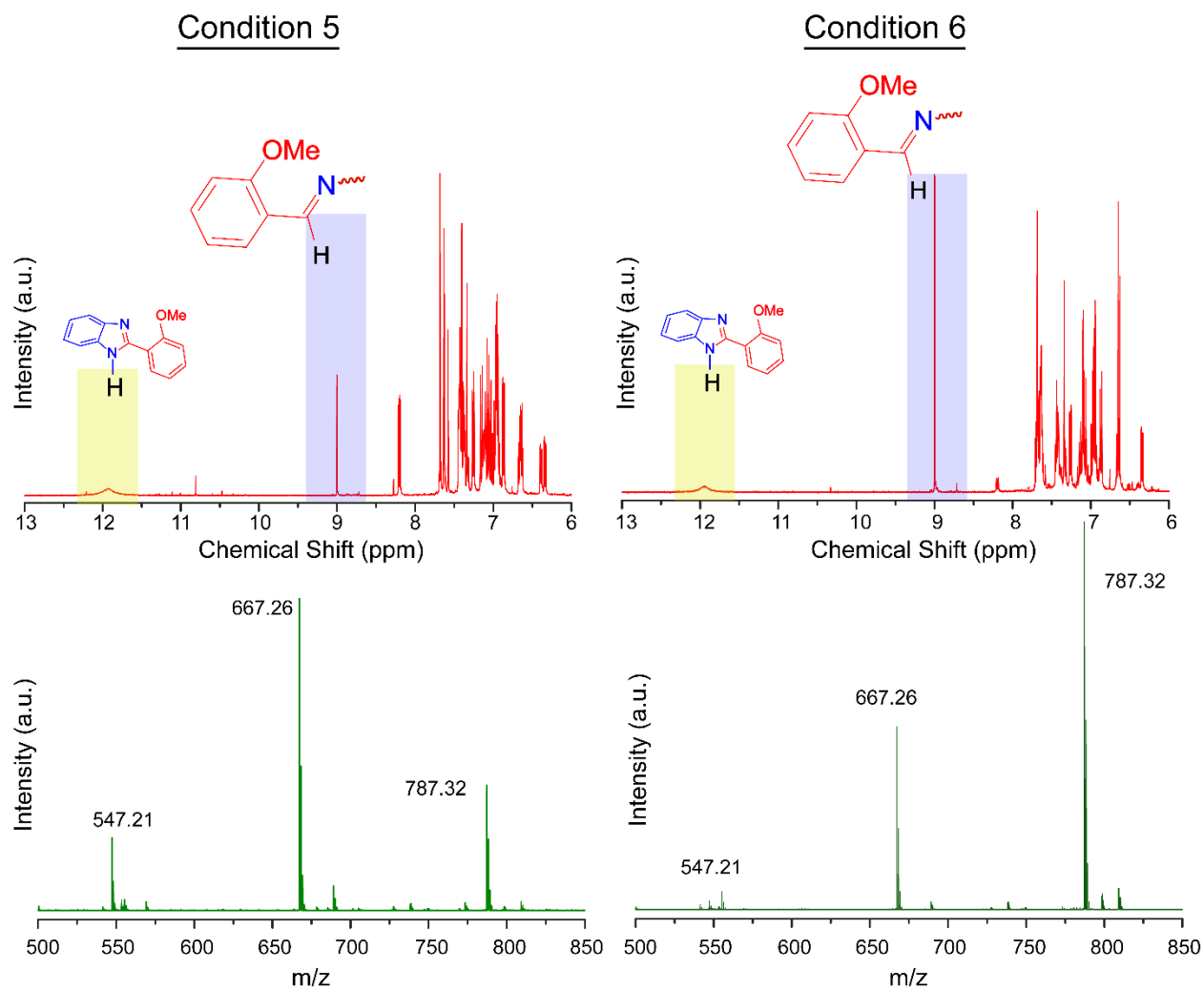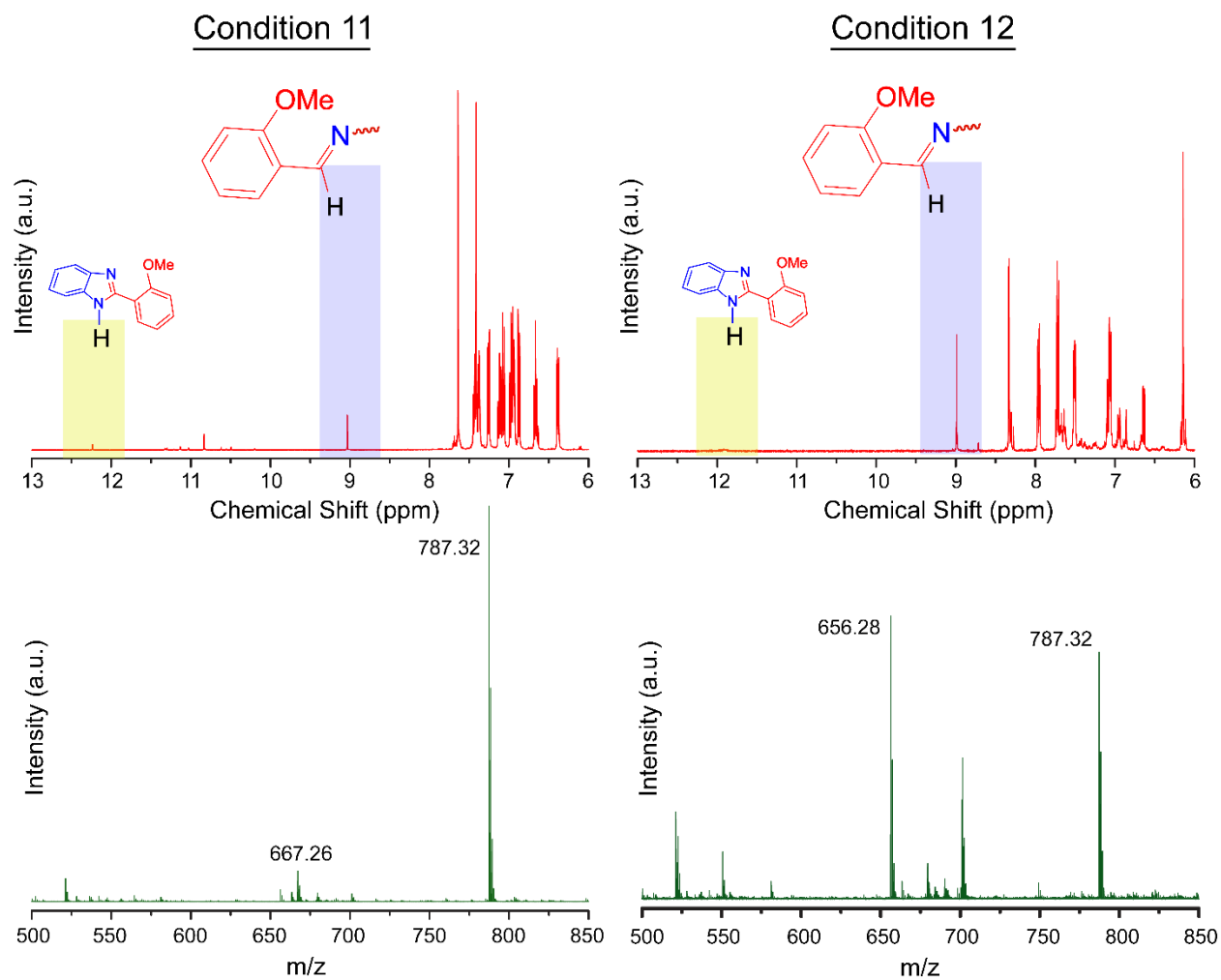
Supplementary Figure 5: Calculation of ratio between Imine and Imidazole bonding from 1H NMR studies (Red) and the ratio between three monomers from HRMS data (Green) of the reaction crude at conditions 5 and 6.

Supplementary Figure 6: Calculation of ratio between Imine and Imidazole bonding from 1H NMR studies (Red) and the ratio between three monomers from HRMS data (Green) of the reaction crude at conditions 7 and 8.

Supplementary Figure 7: Calculation of ratio between Imine and Imidazole bonding from 1H NMR studies (Red) and the ratio between three monomers from HRMS data (Green) of the reaction crude at conditions 9 and 10.

Supplementary Figure 8: Calculation of ratio between Imine and Imidazole bonding from 1H NMR studies (Red) and the ratio between three monomers from HRMS data (Green) of the reaction crude at conditions 11 and 12.

Section 3: FT-IR Spectra
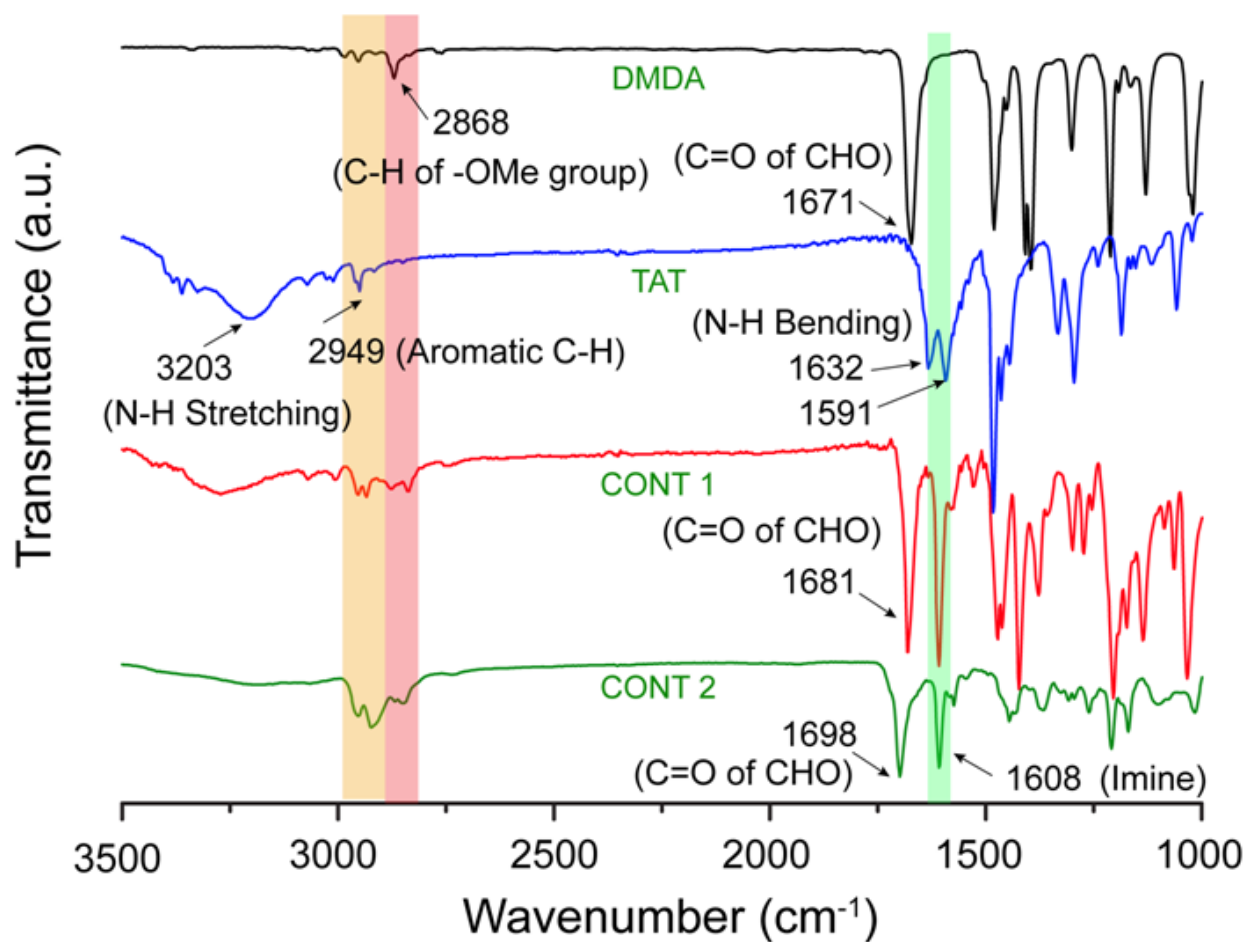
Supplementary Figure 9: Comparison of FT-IR spectra between as-synthesized CONT-1 and CONT-2 with the starting materials (aldehyde and amine)/structural building units. FT-IR Spectra suggests free aldehyde functionalities of CONTs, which could be generated from the defects. Both the spectra of CONT-1 and CONT-2 also show characteristic peaks corresponding to the imine-linked framework structure.

Section 4: Solid-State NMR Spectra
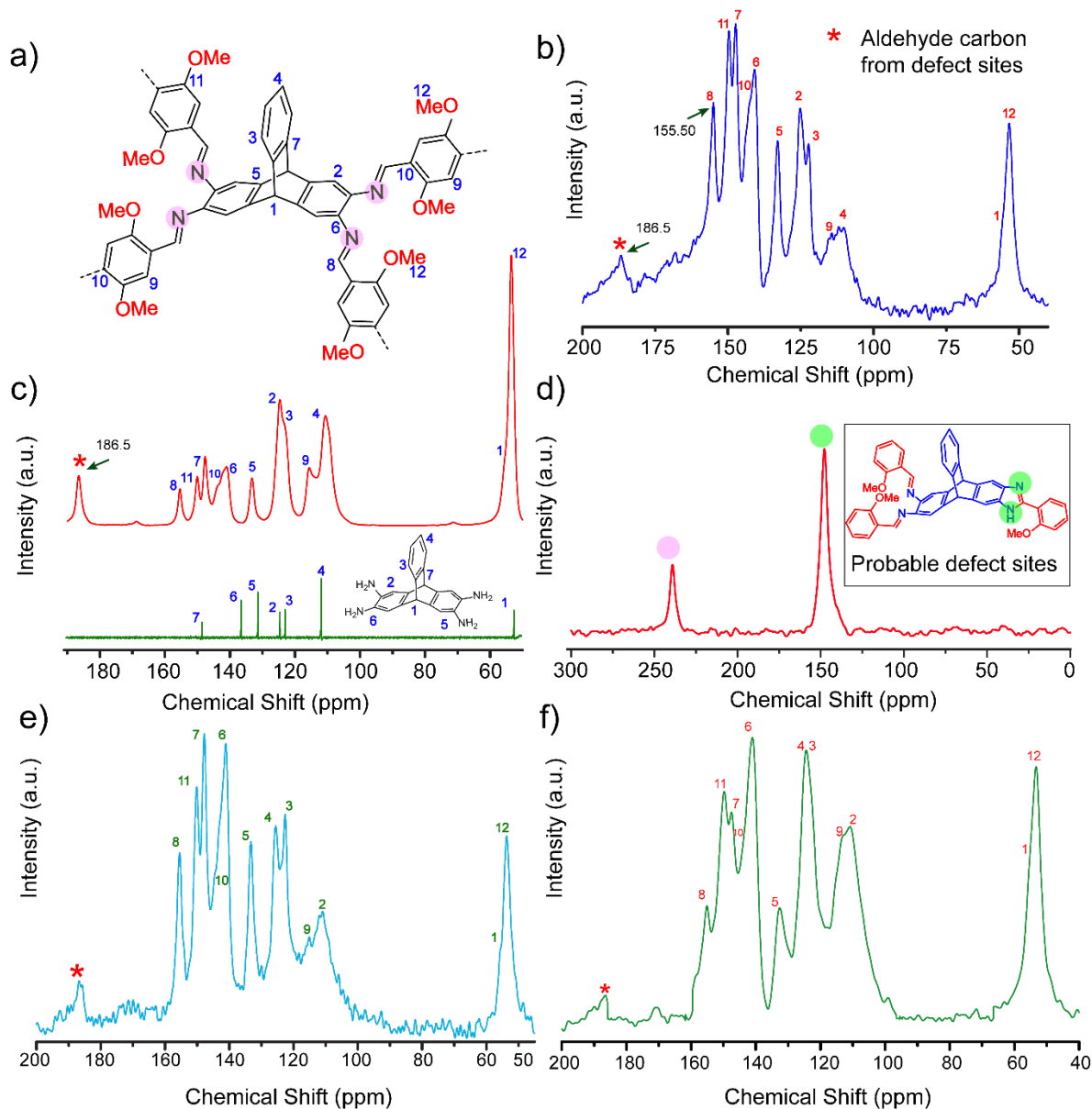
Supplementary Figure 10: a) Repeating unit of the covalent organic nanotube (CONT-1). b) Solid-state High-Power Decoupled (HPDEC) ^{13}C NMR spectra of the CONT-1 for quantitative analysis of different groups (carbon atoms with probable chemical shift mentioned with numerical in Chem Draw). c) Solid-state ^{13}C CP-MAS spectra of synthesized CONT-1 (carbon atoms with probable chemical shift mentioned with numerical in Chem Draw) along with solution-state ^{13}C NMR of TAT. d) Solid-state ^{15}N CP-MAS spectra of CONT-1. e) & f) Solid-state High-Power Decoupled (HPDEC) ^{13}C NMR spectra of the 150 mg and 280 mg CONT-1 respectively synthesized from different batches of reactions.

15

According to the reaction scheme, the basic unit consists of 20 carbons from TAT and 10x4=40 carbons from DMDA. Out of these, 18 carbons from TAT and 32 carbons from DMDA appear in the aromatic and carbonyl region (200 to 100 ppm), and two carbons of TAT and eight carbons of DMDA appear in the aliphatic region (~60 ppm). Thus, if the reaction is complete, an aromatic to the aliphatic ratio of 5:1 is expected. The ratio obtained from the ^{13}C HPDEC spectrum is approximately the same. Peaks around 186 ppm in the ^{13}C spectra suggest the presence of defects in the structure.

The peak around the 240 ppm in the solid-state ^{15}N spectra indicates the presence of an imine (C=N) bond. However, the peak around 148 ppm seen in the ^{15}N NMR corresponds to =NH. Such =NH moiety comes from imidazole, which can be formed at the defect centers.

## Section 5: N_2 Adsorption Isotherm
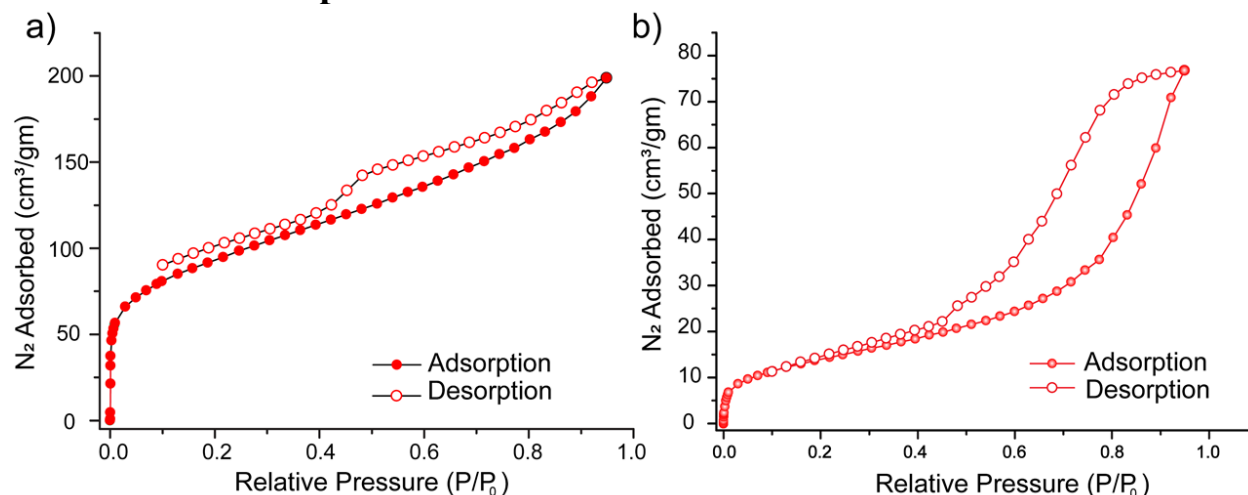
Supplementary Figure 11: N_2 adsorption experiment of the purified and isolated (a) CONT-1 and (b) CONT-2. From the isotherm, the surface area (S_{BET}) of the CONT-1 and CONT-2 were calculated to be 321 m^2g^{-1} and 52 m^2g^{-1}, respectively.
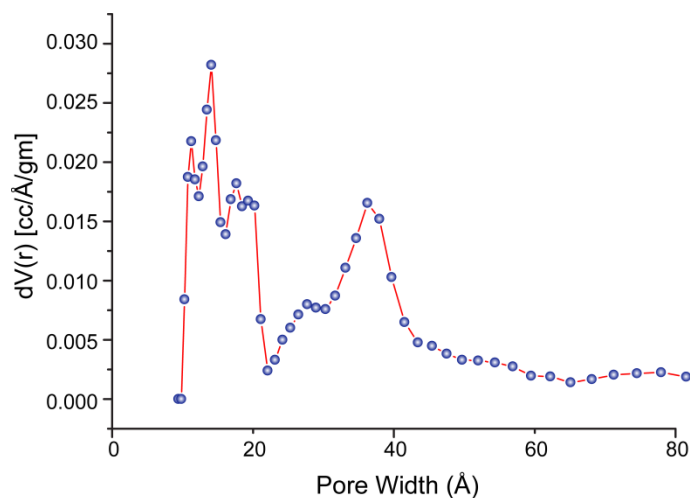

Supplementary Figure 12: The pore size distribution of the CONT-1 obtained from the N_2 adsorption experiment. Pore size distributions were calculated using the nonlocal density functional theory (NLDFT) model.

Section 6: SEM Images of Isolated CONT-1
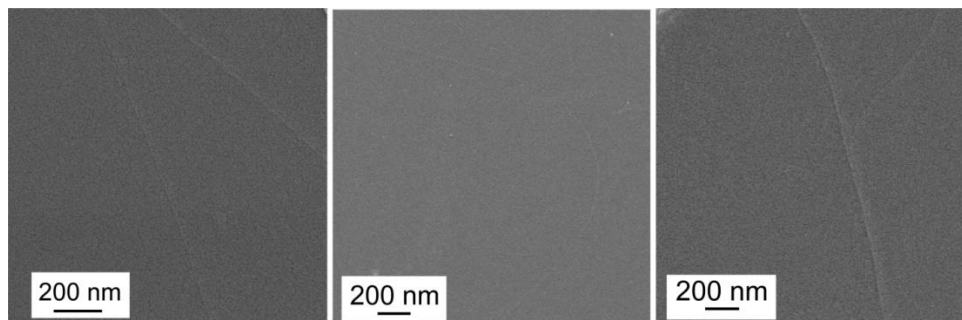
Supplementary Figure 13: SEM images of single isolated CONT-1. It shows the length of these nanotubes in the micrometer range with a uniform diameter of ~5nm.

Section 7: TEM Images of Isolated CONT-1
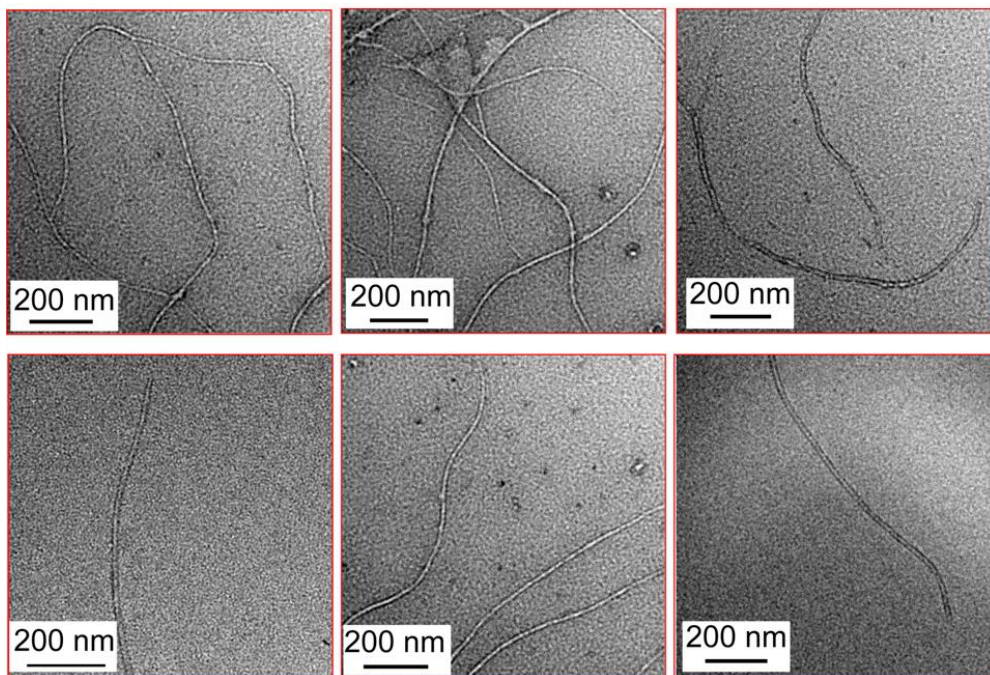
Supplementary Figure 14: TEM images of isolated CONT-1. The hollow interior confirms the tubes' diameter on the sub-10-nanometer scale, ~5 nm.

The hollow interior length (the white part only in TEM images) varies from 4 to 6 nm, which could be due to moderate resolution, sample preparation, and scale measurement errors. Here, we have considered an average of 5 nm as the inner diameter of the CONTs.

Section 8: AFM Images of Isolated CONT-1
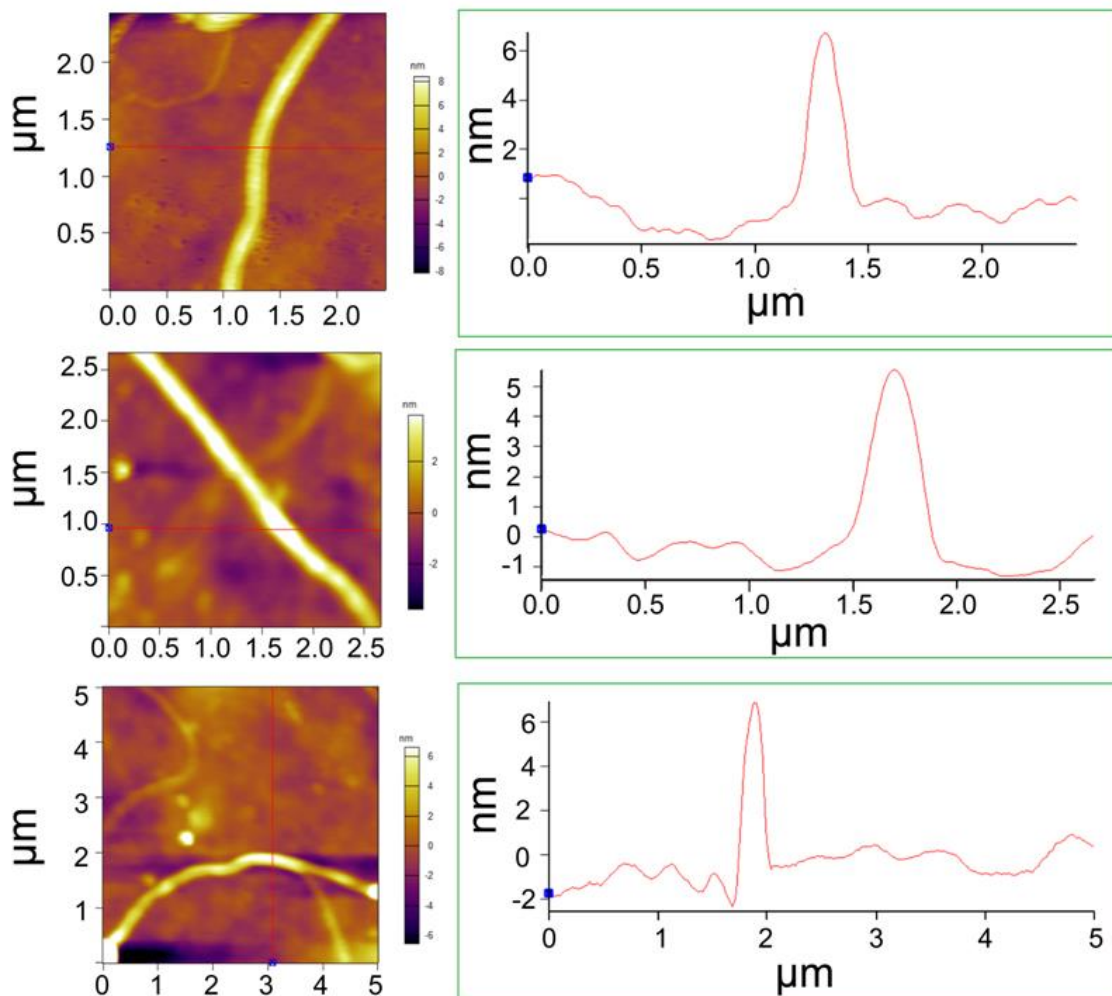
Supplementary Figure 15: AFM images of the single covalent organic nanotubes (CONT-1). The height profiles show the uniform average CONT's diameter of ~5 nm.

Like the SEM and TEM images of isolated nanotubes, the AFM also shows nanotubes' height in the range of 5-6 nm. The outer diameter of CONT-1 is ~5 nm from the AFM height profile, reasonably expected in single-walled- covalent organic nanotubes.

Section 9: Time-Dependent Morphology Study of CONT-1
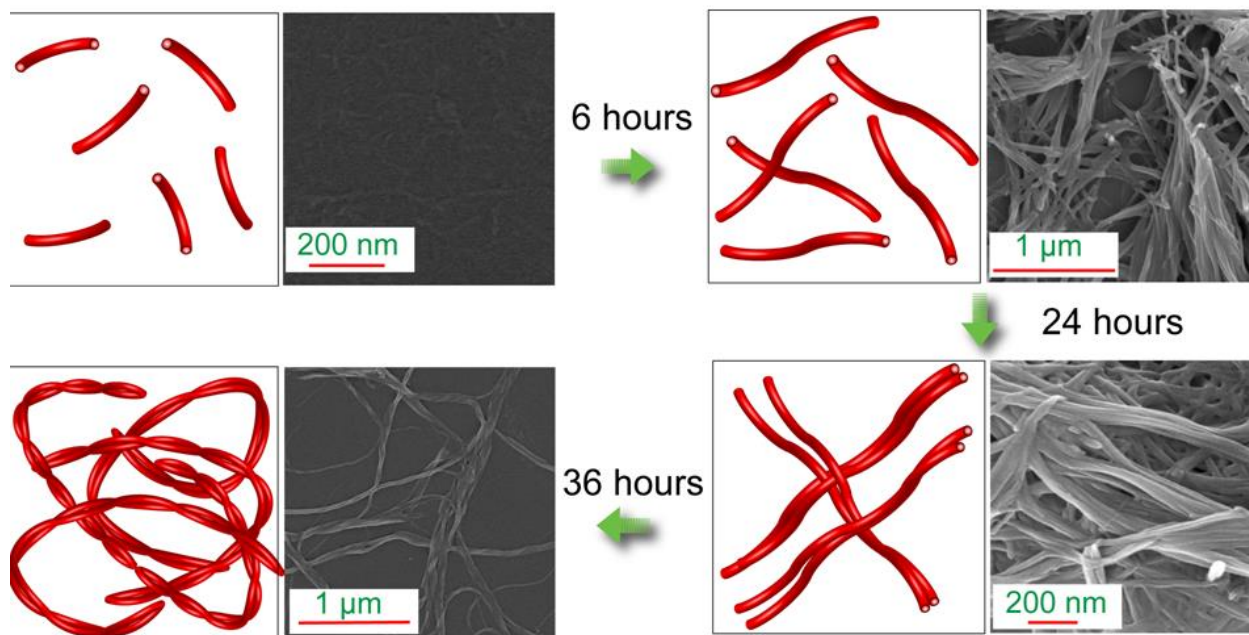
Supplementary Figure 16: Time-dependent study of nanotube (CONT-1) formation via SEM imaging.

We have isolated the reaction mixtures at different time intervals and characterized them *via* SEM analysis to shed more light on the CONT-1 formation (Supplementary Figure 16). CONT-1 formation starts within 6 hours of reaction. However, they are 100-200 nm in length, with a ~5 nm diameter. The length gradually increases without significant alteration of their diameter. After 12 hours, the CONTs grow up to 500-800 nm in length with a diameter of ~5 nm (avg. length to diameter ratio 130:1). The intertwining starts after 24-30 hours when the length to diameter ratio of the CONTs increases significantly (~avg. 200:1). The rapid increase in the length of CONTs induces high flexibility, promoting the formation of intertwined structures. After 36 hours of reaction, almost all CONTs become completely intertwined, and no significant morphological changes were observed further.
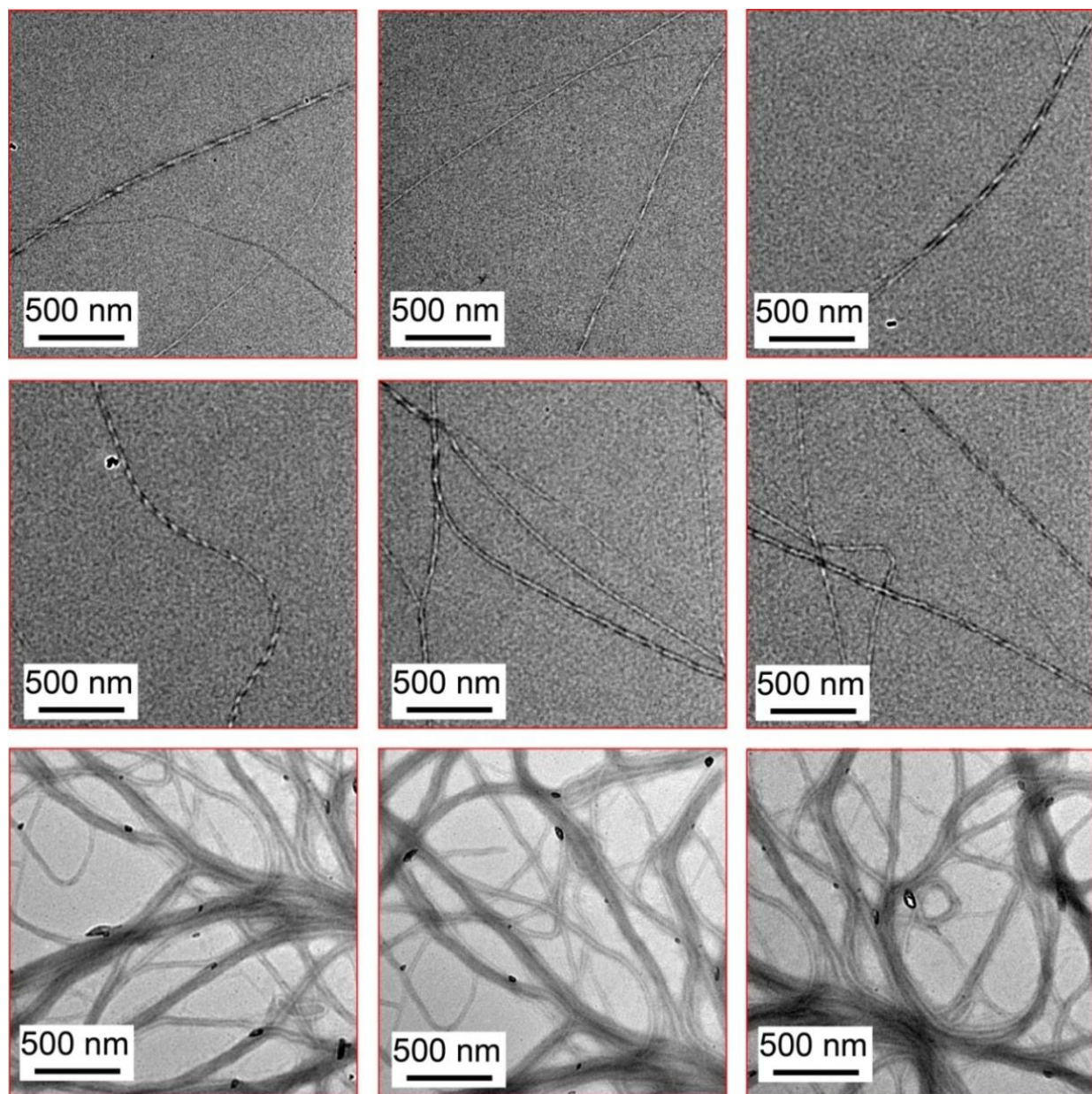
Section 10: SEM Images of Intertwined CONT-1
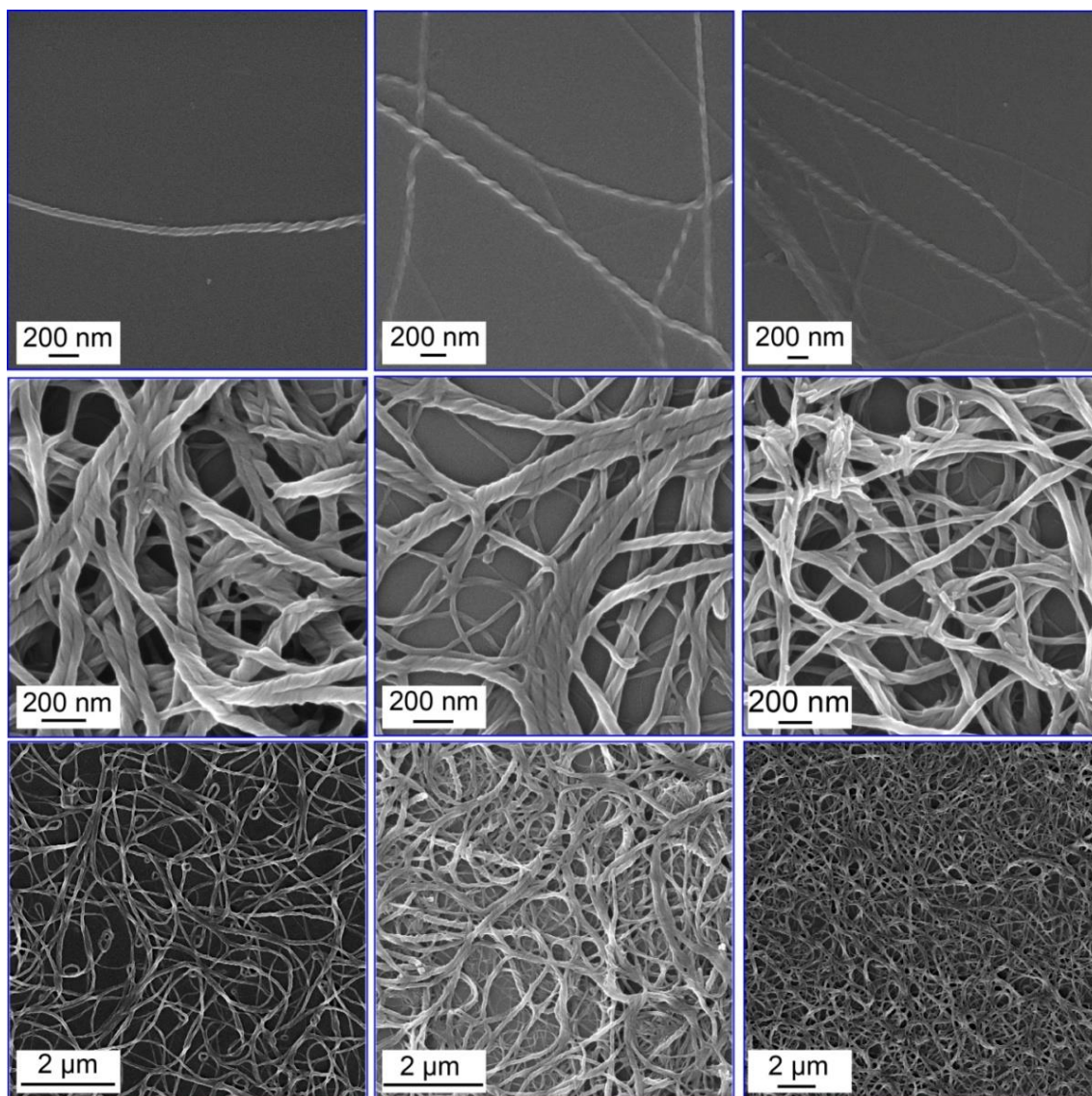
Supplementary Figure 17: SEM images of intertwined covalent organic nanotubes (CONT-1).

The extent of intertwining depends on many factors, including solvents, concentration, and amounts of defects. In dilute solution, the CONT-1 is less intertwined as the availability of neighboring CONTs is less. We believe that the intertwining is triggered (initiated) by defects in the CONT-1 backbone. However, the regulation and precise pitch of intertwining somewhat dismissed the sole role of defects. The theoretical studies showed the effect of solvent as well. So, the intertwining is resulting from the combined effects of defects and solvents.

Section 11: TEM Images of Intertwined CONT-1

Supplementary Figure 18: TEM images of the intertwined covalent organic nanotube (CONT-1). Two flexible CONTs interconnect first at a single point. This leads in time to the formation of intertwined structures with a constant pitch. The convoluted CONTs then hierarchically generate network-like superstructures.

Section 12: Pitch of Intertwined CONT-1

TEM Image:
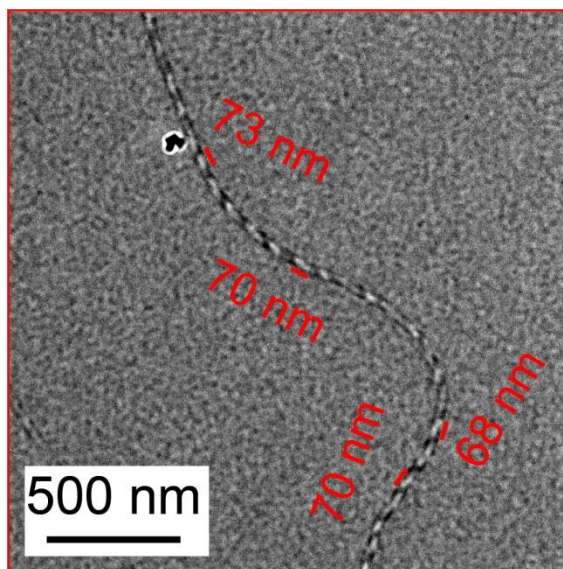
Supplementary Figure 19: TEM image of intertwined CONT-1 shows the uniform pitch of 70 ($\pm$10) nm.

AFM Image:
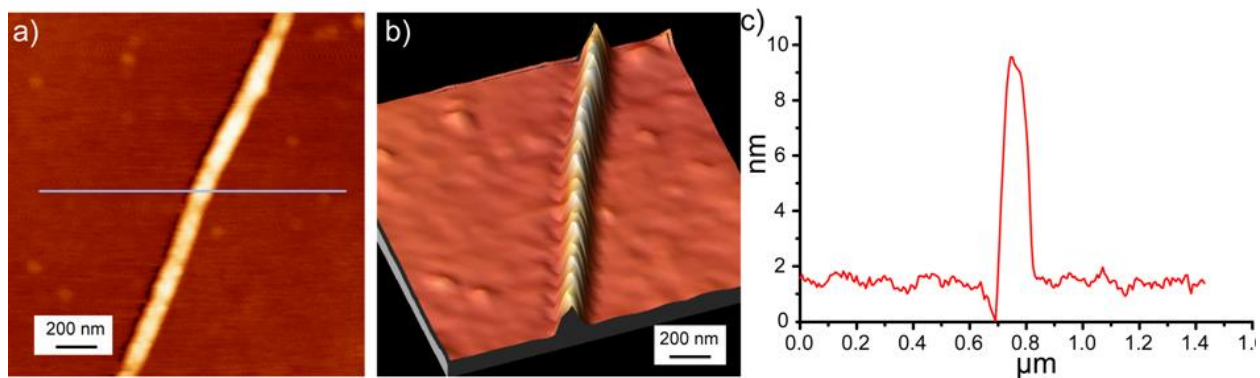
Supplementary Figure 20: a) 2D AFM image b) 3D AFM image of intertwined CONT-1 shows the uniform pitch of 70 ($\pm$5) nm. c) The height profile confirms the presence of two nanotubes.

Section 13: AFM Images of Intertwined CONT-1
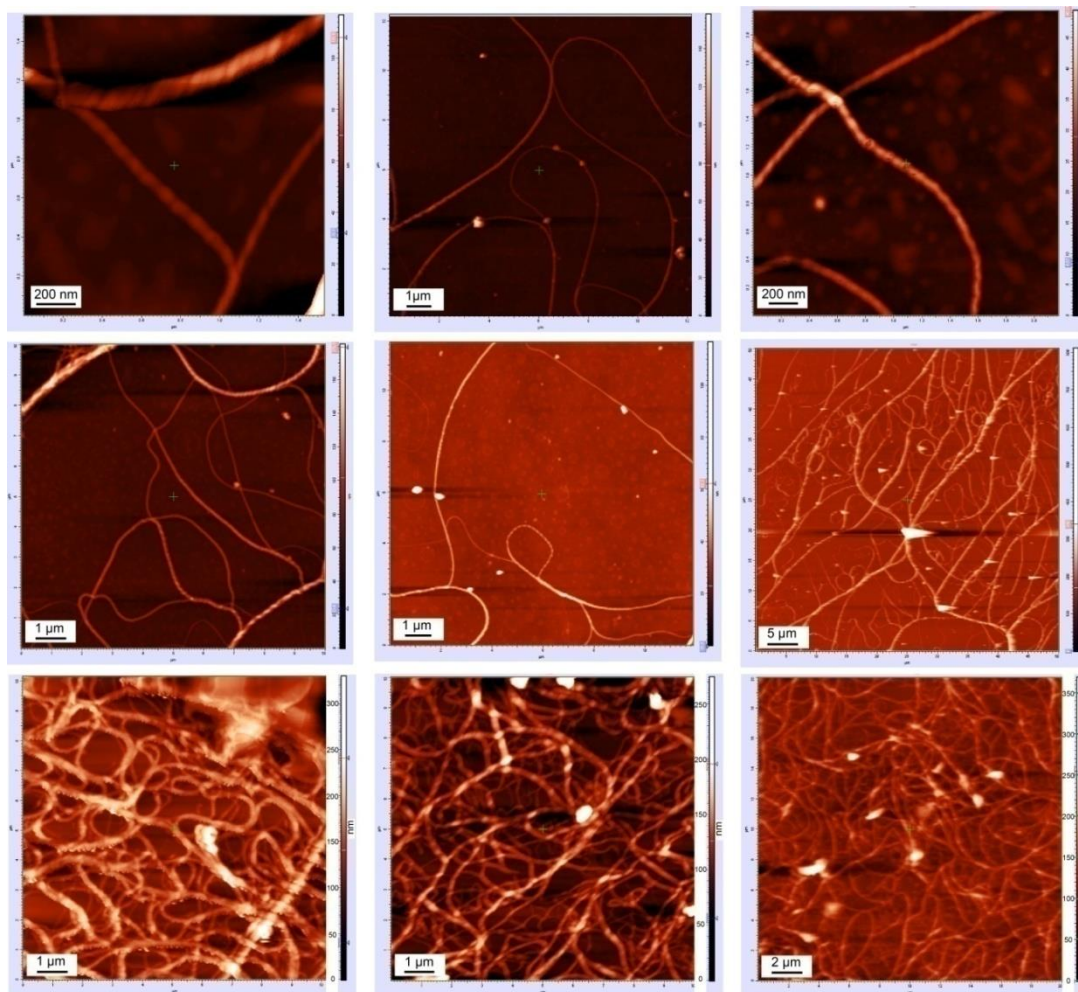
Supplementary Figure 21: AFM images of the covalent organic intertwined nanotubes.

Section 14: SEM Images of CONT-2
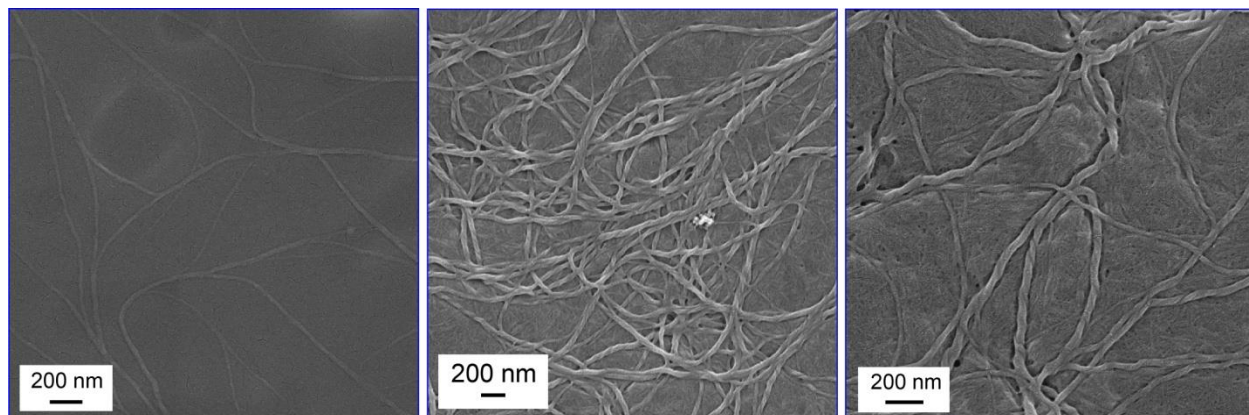
Supplementary Figure 22: SEM images of the covalent organic nanotubes (CONT-2).

Section 15: TEM Images of CONT-2
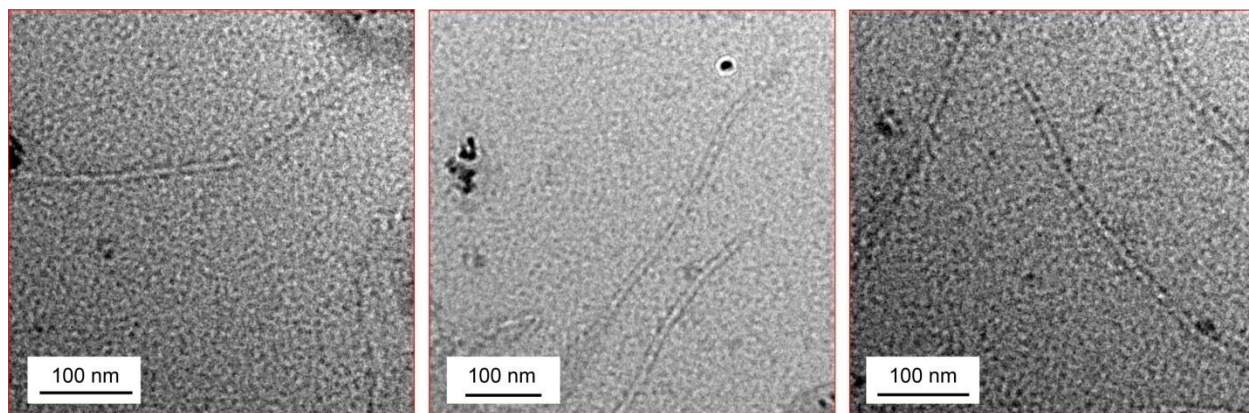
Supplementary Figure 23: TEM images of the covalent organic nanotubes (CONT-2).

Section 16: Defects in Covalent Organic Nanotubes
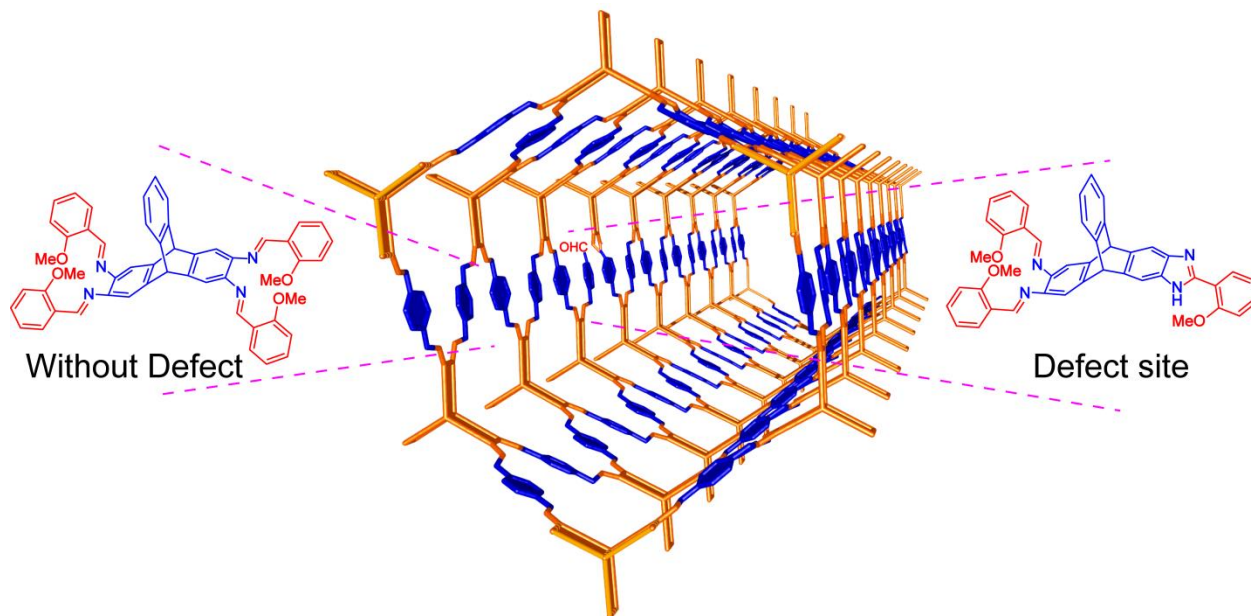
Supplementary Figure 24: Probable defect sites in covalent organic nanotubes due to imidazole ring formation.

The defect centers are generated due to imidazole ring formation between one aldehyde (-CHO) and two amino (NH_2) groups in the presence of O_2.
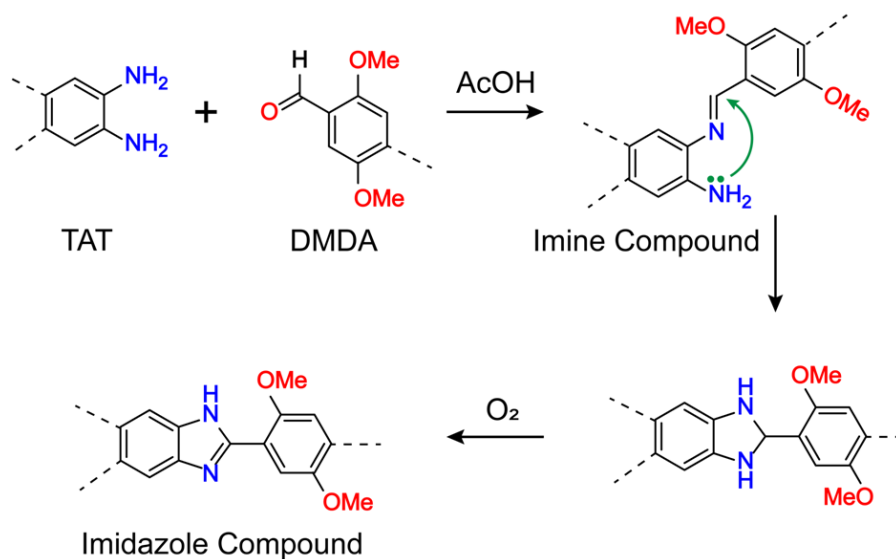
The imidazole ring formation results in one free aldehyde group (-CHO) in the CONT's framework (Supplementary Figure 24). These –CHO groups appear in the solid-state ^{13}C CP-MAS NMR spectra (Supplementary Figure 10c). The Solid-state High-Power Decoupled (HPDEC) ^{13}C spectrum NMR spectrum quantifies the amount of –CHO group is 6-8% equal to the framework's defect centers (Supplementary Figure 10b).

Section 17: Separation of Toroids from CONT-1
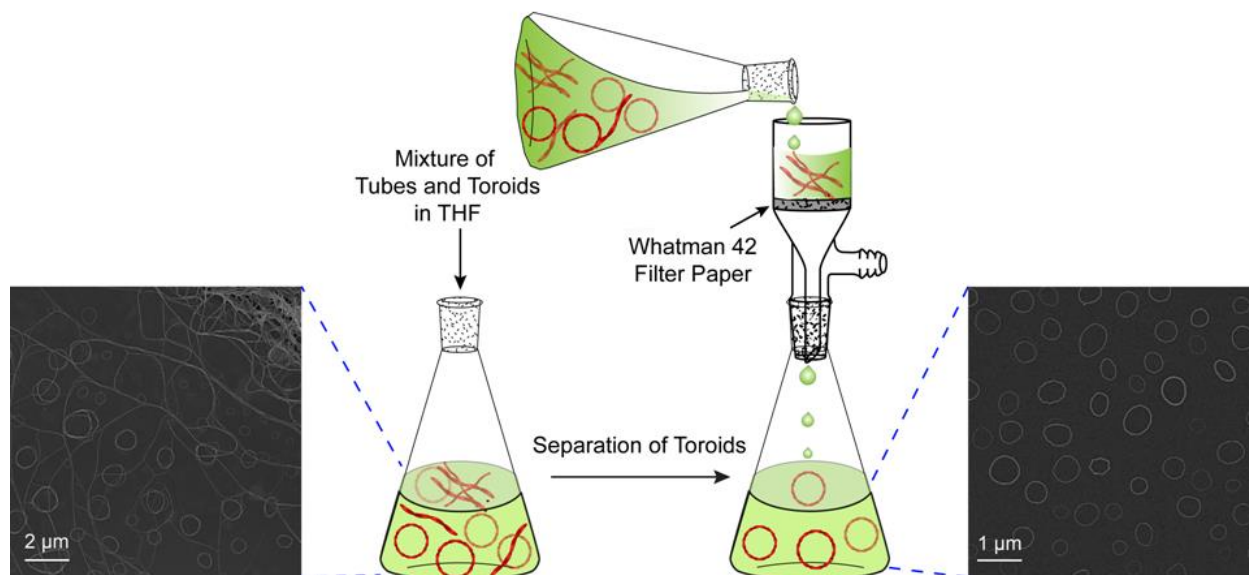
Supplementary Figure 25: Schematic representation of separation procedure of Toroids from the mixture of CONT-1 and Toroids.
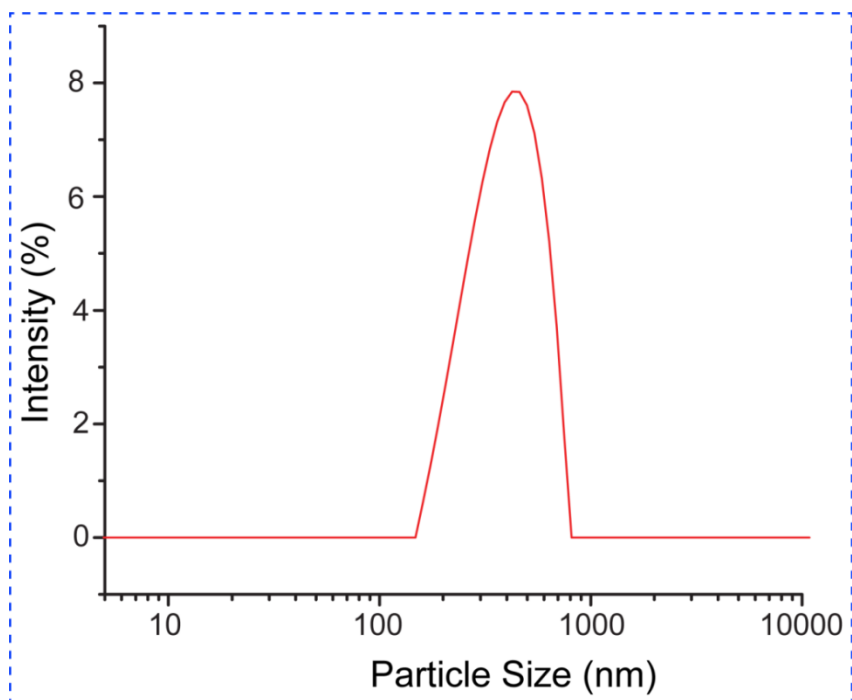
Supplementary Figure 26: DLS study of the toroids formed from covalent organic nanotubes shows a hydrodynamic diameter of ~652 nm and PDI=13.5%.

Section 18: SEM Images of Toroids
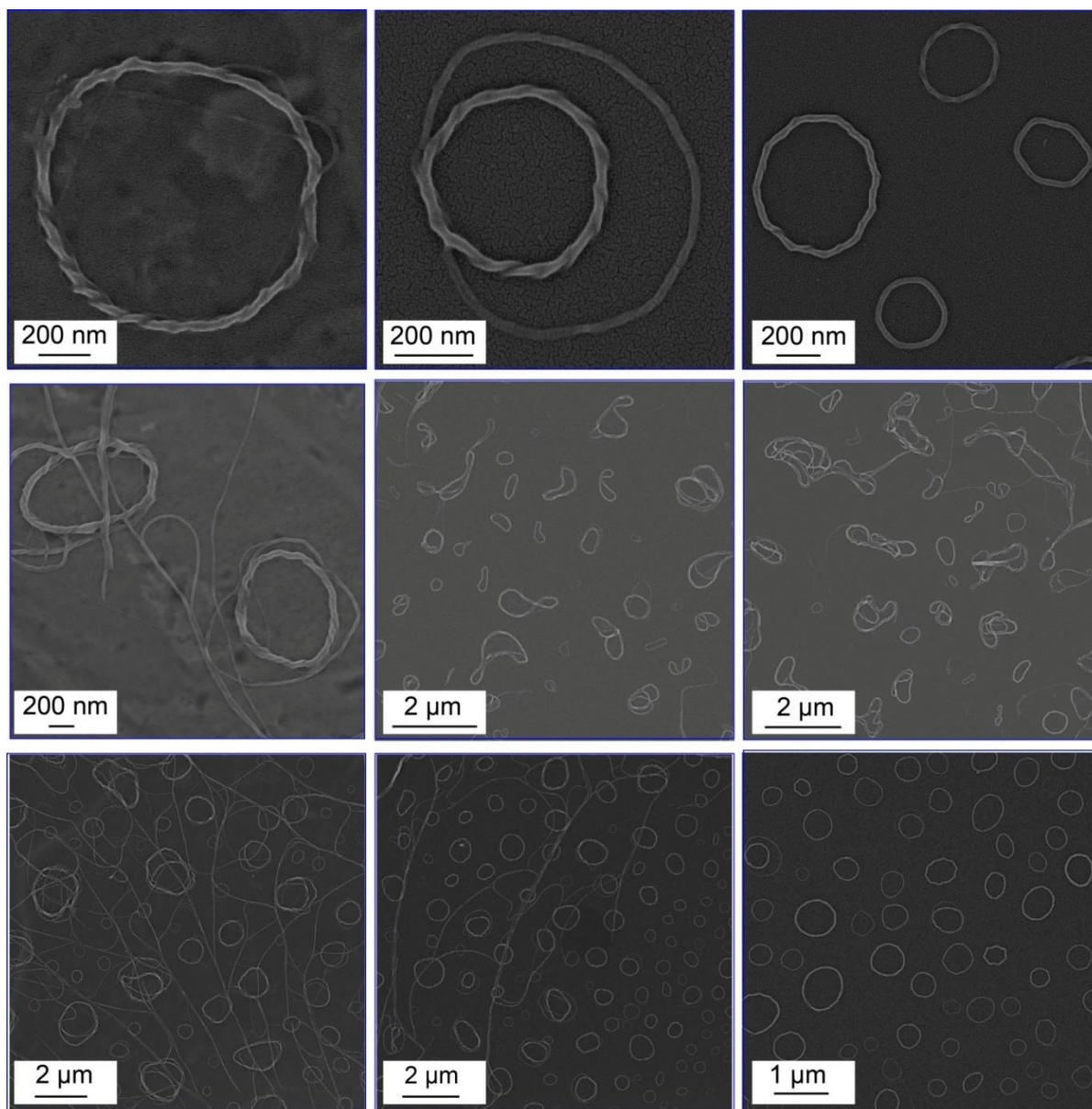
Supplementary Figure 27: SEM images of the covalent organic toroids.

2 mg intertwined CONT-1 was taken in 50 mL anhydrous THF and sonicated at room temperature. 20 µL of the finely dispersed solution was drop-casted on a silicon wafer or TEM grid. The intertwined nanotubes are coiled to form circular micro rings with a diameter ranging from 300 nm to 900 nm.

Section 19: TEM Images of Toroids
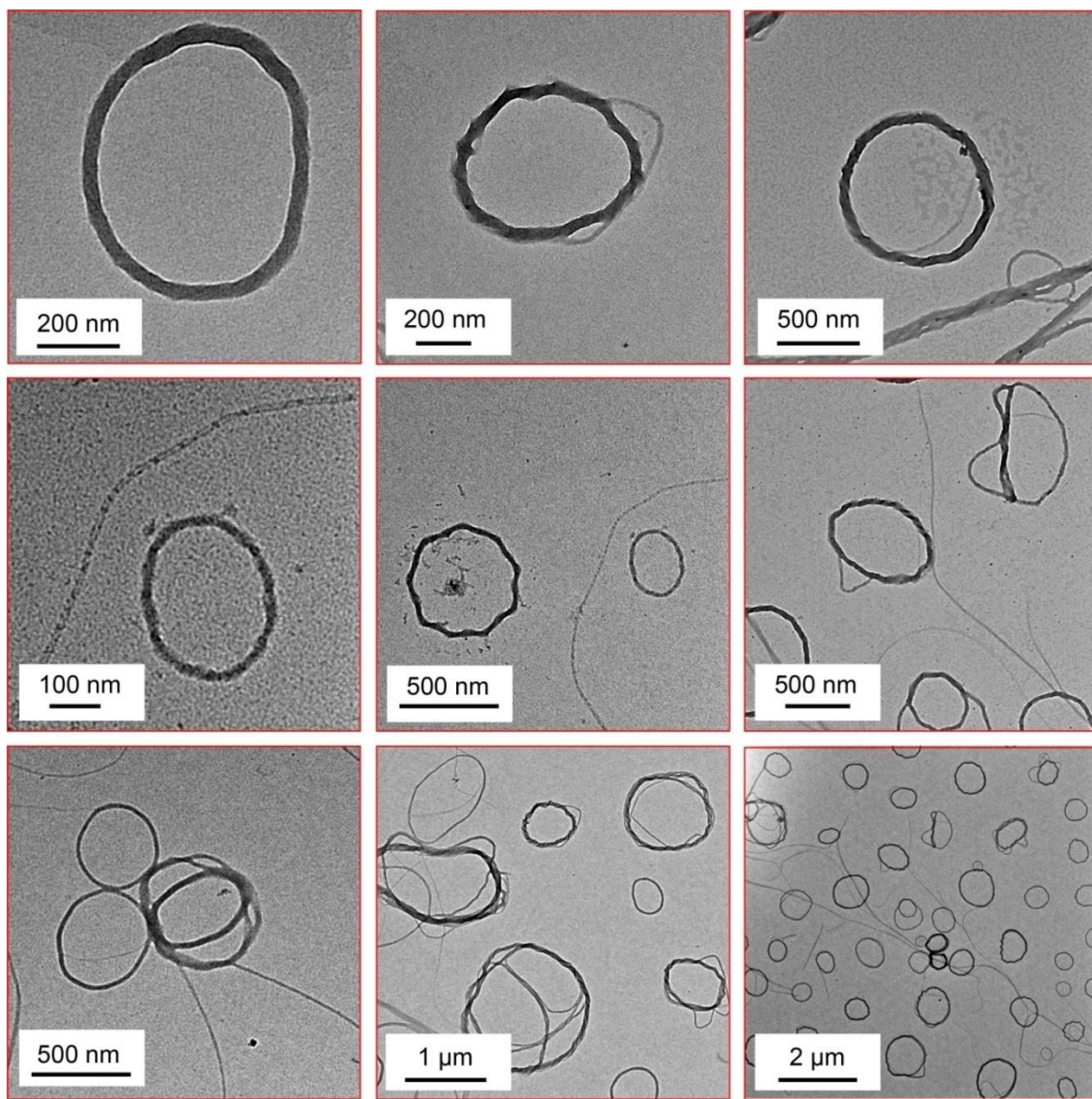
Supplementary Figure 28: TEM images of the covalent organic toroids.

The most probable mechanism involves the creation of bubbles in THF. The bubbles act as the template for hydrophobic CONT-1, which eventually orient themselves around such bubbles' circumference. Being bent at the bubble–THF interface, nano-tubes form loops when the bubble collapses. The untied twinned nanotubes coil up to create a closed and coiled loop-like structure with varying diameters (0.1-1 µm). These spiral loop structures were later transformed into toroidal structures.

Section 20: AFM Images of Toroids
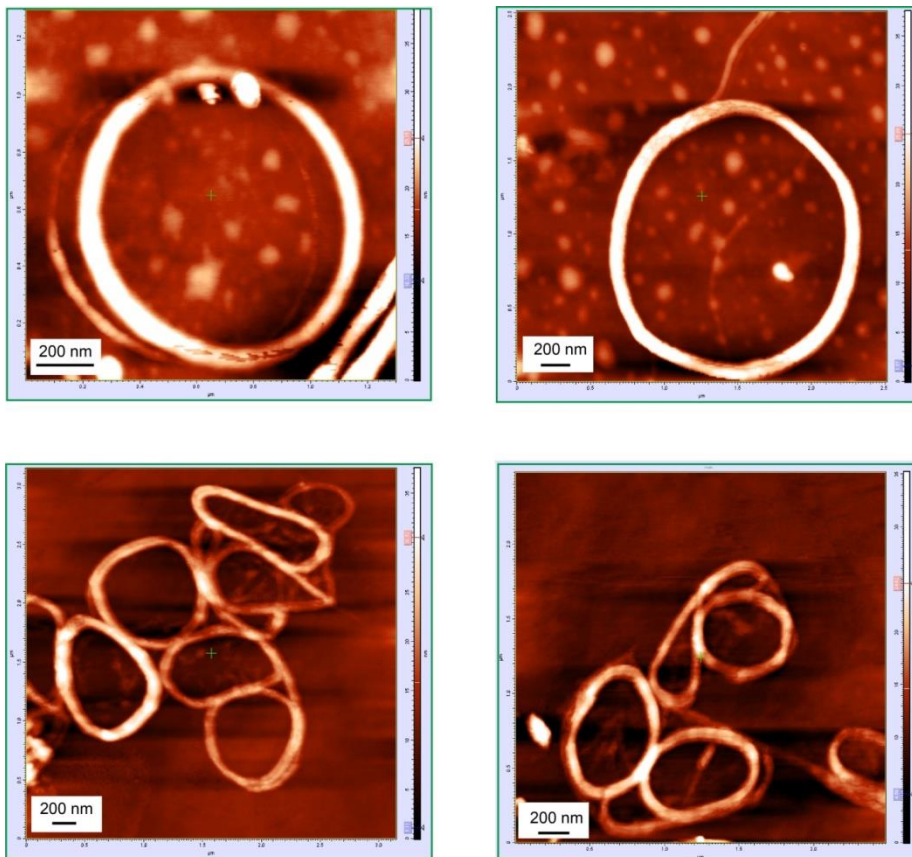
Supplementary Figure 29: AFM images of the covalent organic toroids.

Section 21: Mechanism of Toroid formation from Intertwined CONTs
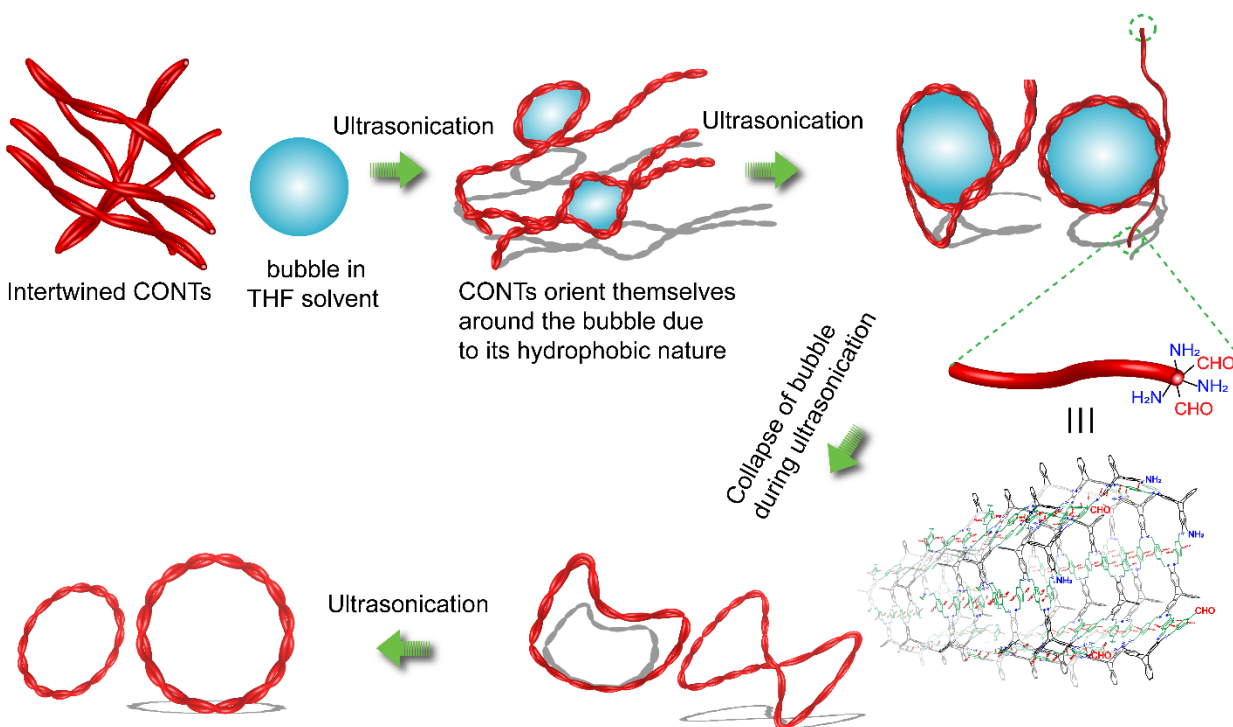
Supplementary Figure 30: Probable mechanism of Toroids formation from intertwined nanotubes. The bubble formation in THF assists CONTs to form a loop, which eventually leads to toroid formation.

we believe that the probable mechanism of toroid formation also involves bubble generation in THF. The bubbles act as the template for hydrophobic CONTs, which eventually orient themselves around such bubbles' circumference. Being bent at the bubble–THF interface, nanotubes form loops when the bubble collapses. The untied intertwined nanotubes coil up around the bubble in both the transverse and longitudinal directions to create a closed and coiled loop-like structure of various diameters (0.1-1 µm). These spiral loop structures were later transformed into toroidal structures (Supplementary Figure 30). SEM, TEM, and AFM images show the end part of the intertwined nanotube present at the periphery of distorted toroids. However, there is no open part of the nanotube in the final toroids. These suggest that the free aldehyde and amine groups at the end of the nanotube structure react to form an imine bond via Schiff base condensation close the loop.

Section 22: Calculation of Yield of Toroids
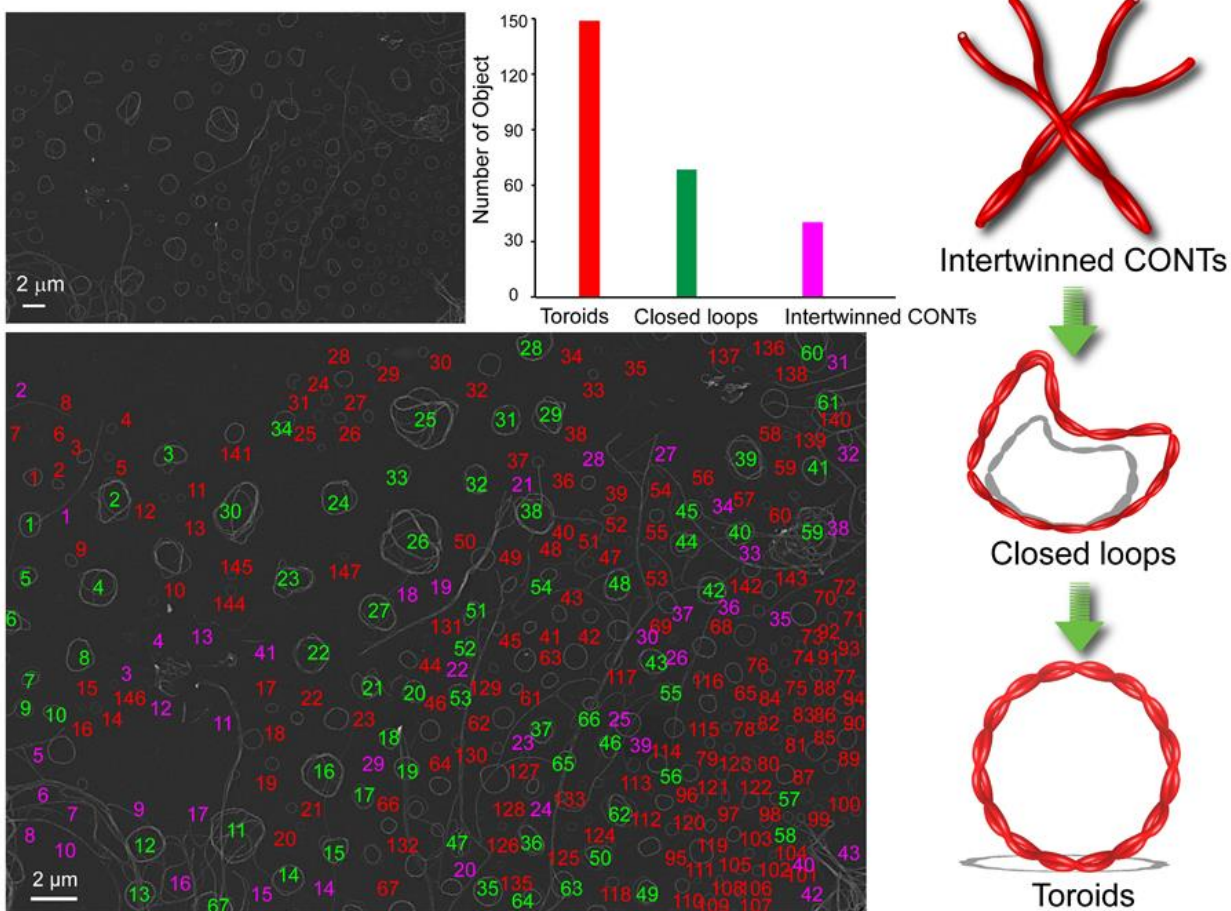
Supplementary Figure 31: Estimation of the yield of toroids in a complex mixture of the toroid, closed loops, and intertwined nanotubes obtained by drop-casting 10 µL of finely dispersed CONT-1 solution in Tetrahydrofuran (THF). The area of the SEM image is 35 µm X 25 µm.

Section 23: Comparison of Properties between Toroids and Nanotubes

Although the chemical properties of toroids and intertwined CONTs are expected to be the same due to their similar chemical bonding, the physical properties could be different because of their different dimensionality and assembly. To compare chemical properties, we have performed TGA analysis of toroids and intertwined CONTs (Supplementary Figure 32). Both Toroids and CONTs are stable up to ~400 ℃. The close thermal stability indicates their similar chemical properties.
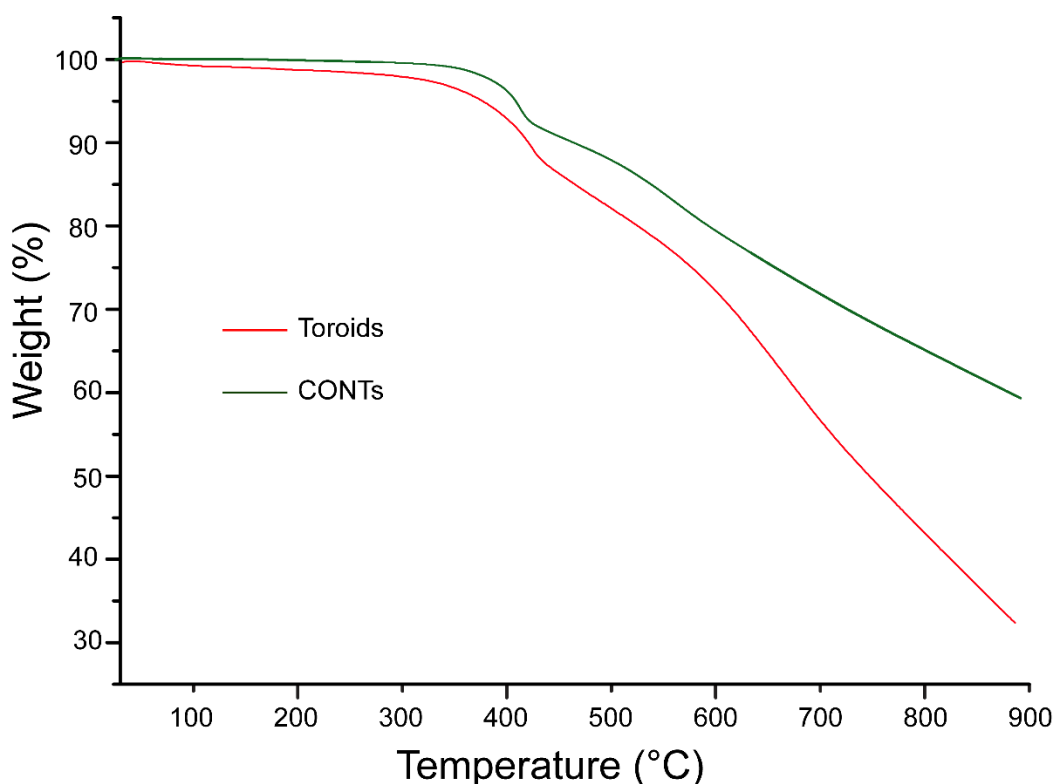
Supplementary Figure 32: Comparison of thermal stability of Toroids and CONTs. The TGA analysis of both toroids (Red) and CONTs (Green) show similar thermal stability (up to 400 ℃).

To compare their physical properties, we have checked the dispersion stability of both toroids and intertwined CONTs by Tyndall effects (Supplementary Figure 33). The toroids are much more stable than intertwined CONTs. Higher dispersion stability is required for biomedical applications like drug delivery and device fabrication for various electronic applications.

Dispersion stability of Toroids
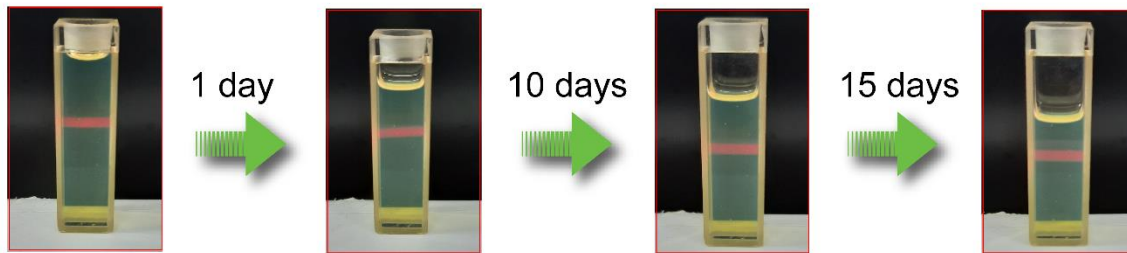
Dispersion stability of CONTs
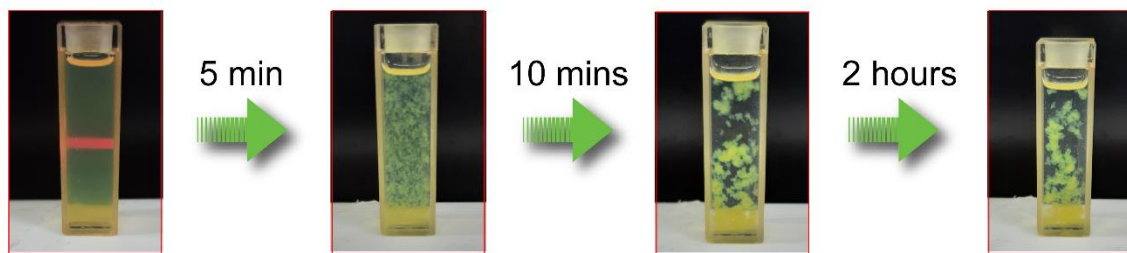
Supplementary Figure 33: Comparison of physical properties of Toroids and CONT-1. The dispersion stability of toroids is much higher than that of CONTs. The well-dispersed toroid solution is stable for more than one month. In contrast, the intertwined CONTs precipitate out in 10 minutes.

Section 24: TGA Data of CONTs
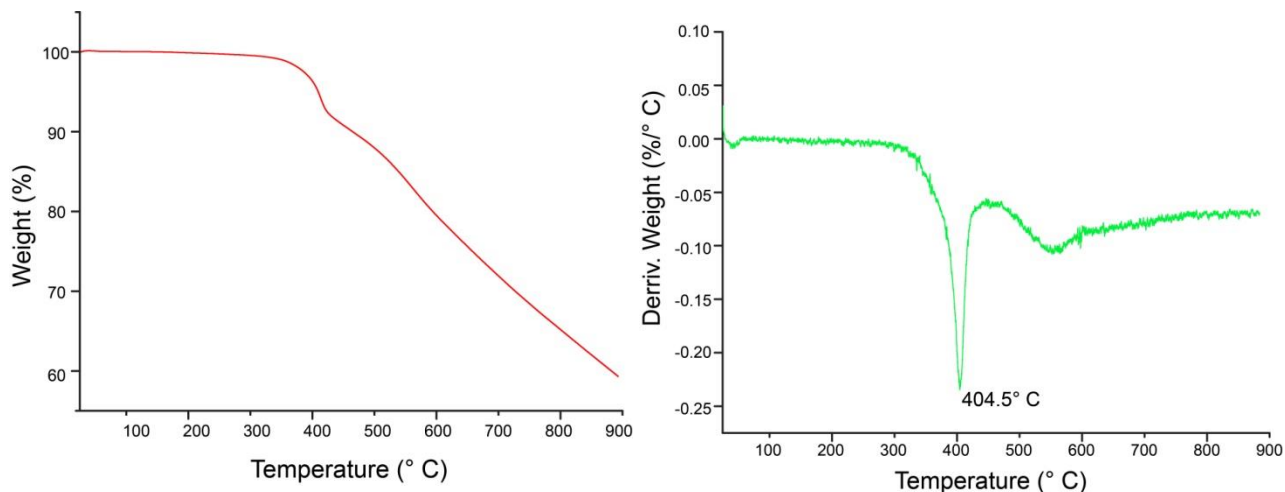
Supplementary Figure 34: TGA of the CONT-1 (after activation of the sample). The analysis shows that the porous covalent organic nanotubes have very high thermal stability and are stable up to ~400 °C. This high thermal stability comes from the resonance effect of the –OMe group ortho to imine bond.[3]
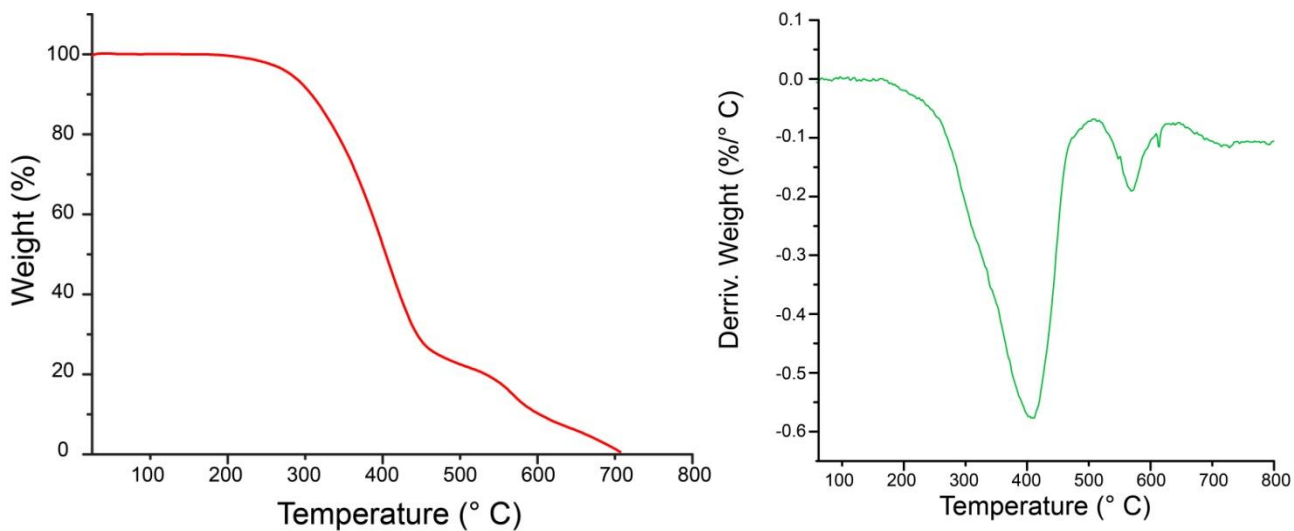
Supplementary Figure 35: TGA of the CONT-2 (after activation of the sample). The analysis shows the material is starting to degrade from 240 ℃. This lower thermal stability can be explained by considering the poor stability of the imine bond. Other groups do not stabilize this imine bond, like CONT-1, where the –OMe group stabilized the imine bond.

Section 25: Stability of CONT-1

Water Stability:

To check the water stability, 20 mg CONT-1 was taken in a beaker, and 50mL distilled water was added at room temperature. The dispersed solution was kept for seven days. After that, the CONT-1 is separated by filtration, dried, and activated for N_2 adsorption isotherm.
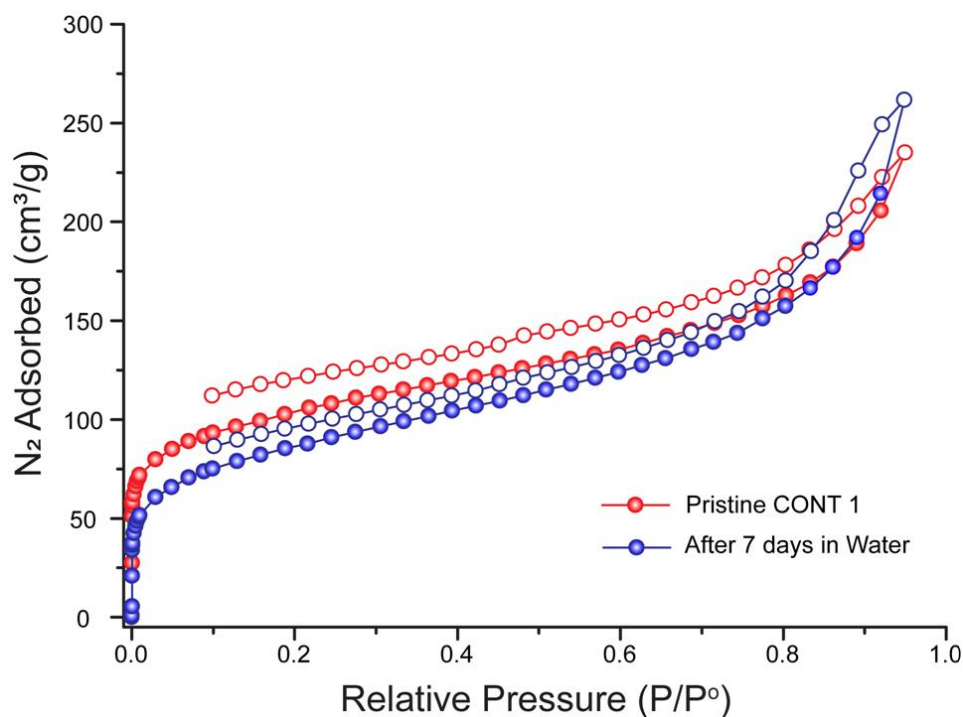
Supplementary Figure 36: N_2 adsorption experiment of the purified and isolated CONT-1 (red) and CONT-1 after water treatment for seven days (blue). From the isotherm, the surface area (S_{BET}) of the CONT-1 before and after water treatment were calculated to be 341 m^2g^{-1} and 294 m^2g^{-1}, respectively.

This high water stability comes from the combined effect of resonance of –OMe group *ortho* to imine bond, which reduces the electrophilic character of imine carbon center to some extent.

Acid Stability:

To check the acid stability, 20 mg CONT-1 was taken in a beaker, and 50 mL 1N hydrochloric acid (HCl) was added at room temperature. The dispersed solution was kept for seven days. After that, the CONT-1 is separated by filtration, dried, and activated for N_2 adsorption isotherm.
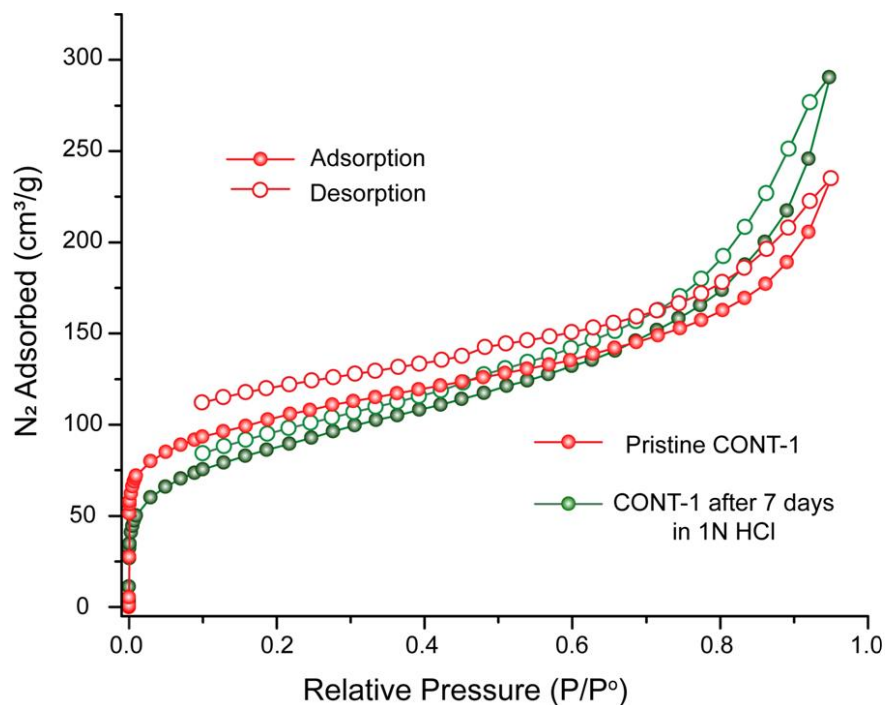
Supplementary Figure 37: N_2 adsorption experiment of the purified and isolated CONT-1 (red) and CONT-1 after 1N HCl treatment for seven days (green). From the isotherm, the surface area (S_{BET}) of the CONT-1 before and after 1N HCl treatment was calculated to be almost the same.

Section 26: Computational Methods

26.1 All-Atom Modeling

All simulations were performed with the GROMACS 2018 software [4,5] equipped with PLUMED 2.5 for the umbrella sampling simulations and systems analysis.[6, 7]

The AA CONT-1 model was parameterized based on the General Amber Force-Field (GAFF)[8] using the Antechamber software.[9] The partial atomic charges for the tubule were computed using the Restrained Electrostatic Potential (RESP) method on an elementary TAT ring layer (composed of 6 TAT and 12 DMDA units, which, replicated along the main tubule axis, generates the complete tubule structure) after geometry optimization performed using PM6 and Hartree-Fock (with the 6-31g* basis set) levels of theory[10] and the Gaussian 16 software.[11]

The AA tubule models used in the AA-MD simulations of Fig. 5 are composed of 16 TAT layers (plus 3 extra TAT units to saturate the tubule structure), corresponding to a tubule length of ~21 nm. This AA CONT-1 model was simulated in different environment conditions: in the absence of solvent (vacuum), in water, in DCM, or THF solvents. In all these AA-MD simulations, the nanotube was placed in a simulation box with periodic boundary conditions. To prevent the CONT interaction with its periodic images via tubule rotation, we imposed external wall potentials acting on the centers of mass of the tube ends (terminal TAT ring layers) that restrained their position to the initial ones within a cylinder having a $0.2 \, nm$ radius on the XY plane. In this way, the AA tubule model is globally free to relax, and it is free to compress or enlarge along the z-direction, but it cannot rotate perpendicular to the major axis during AA-MD. Preliminary energy minimization of the systems was conducted via steepest-descent and short equilibration cycles with a 0.2 fs timestep. The equilibration AA-MD simulations were 200 ns long for each system and were performed using a timestep of 2 fs. The temperature was maintained at 20 °C and the pressure at 1 atm by means of the v-rescale thermostat[12] and Berendsen barostat[13] using isotropic pressure scaling. As done for other supramolecular systems,[14, 15] the organic solvent molecules DCM and THF used in the AA-MD simulations were also parametrized compatibly with the GAFF force field, while simulations in water used the TIP3P water model.[16] Video examples of the of 10ns-long dynamics of the 16 TAT layers in DCM and water are reported in *CONT_whole_DCM.mp4 and CONT_whole_water.mp4 supplementary video files, respectively.* From these equilibration runs we computed the radial distribution function of the tubule heavy atoms with respect to the water's Oxygen atoms and the DCM's Carbon atoms (see Supplementary Figure 40). From this analysis, we observe that the solvation in DCM is more ordered (for instance, a series of maxima that show the presence of solvation shells), while in water the picture appears more dynamic (i.e., with no clear order in the arrangement of water molecules). This observation is qualitatively corroborated by the attached movies (see Supplementary Movie 1 for DCM solvation and Supplementary Movie 2 for water solvation).

Umbrella sampling calculations were employed to qualitatively estimate the local energy of lateral interaction between two CONTs.[17] For these simulations, two shorter CONT-1 models were used, each composed of 6 TAT ring layers positioned parallel to each other in a simulation box. For

these analyses, AA-MD simulations were conducted in periodic boundary conditions, with the tubes restrained at a fixed distance by means of a harmonic potential acting on the distance between the two CONT-1 centers of mass. This was repeated for 66 runs, each with a different equilibrium distance between the tubes, ranging from 3.5 to 6.5 nm. In these runs, the CONTs were kept in the parallel configuration by using restraining potentials that maintained the center of the nanotube ends within a cylinder of 0.9 nm of radius, in practice allowing the tubes to interact only via their lateral surfaces and preventing their rotation. The force constant of the harmonic potential restraining the distance between the tubes was 10^4 kJ mol^{-1}nm^{-2}. The resulting trajectories were combined through the weighted histogram analysis method[18] to obtain the potential-of-mean-force profile (see, *e.g.,* the profile obtained in explicit DCM solvent in Supplementary Figure 38a). From there, we extracted the tubule-tubule interaction energies shown in Supplementary Figure 38b. While these analyses have a qualitative value, as they refer to the lateral (ideal) local interaction between reduced size tubule portions, this allows to qualitatively compare the relative interaction strength between the tubules in different solvents (Supplementary Figure 38b). The errors were computed using the procedure of Ref. 19.
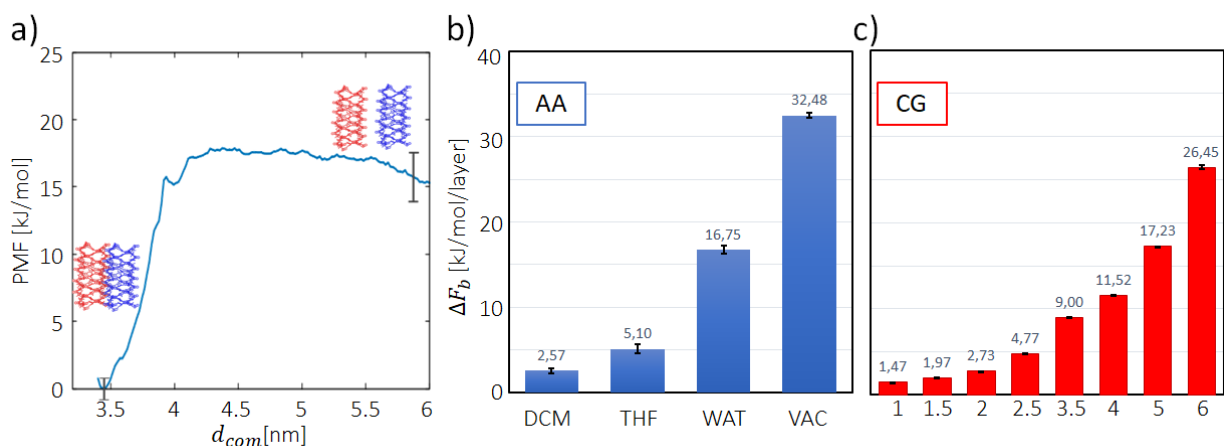
Supplementary Figure 38: CONT-CONT interaction energies in different environments. a) Potential of Mean Force (PMF) profile computed via umbrella sampling for two AA CONT-1 tubes (shown in the insets) immersed in DCM. b) Lateral interaction free energies, ΔF_b, for the AA model in different solvent conditions. The values are indicated per layer units. (c) Free energies of lateral binding for the CG model at different ε values. The free energies of (b) and (c) are obtained via umbrella sampling calculations.

26.2 Coarse-Grained Modeling

The centers of mass of the TAT molecules in the CONT structure were mapped to coarse grained (CG) particles for building a minimalistic CG CONT-1 model, as illustrated in Fig. 5d of the main text. Each CG-bead is connected to 4 other beads, consistently with the geometry of the atomistic CONTs, by means of harmonic potentials of the form:

$$V_b = \frac{k_b}{2}(r - r_0)^2 \tag{1}$$

where r is the distance between two neighboring CG-beads, k_b is the force coefficient, and d_0 is the equilibrium distance of the bond. Angular potentials were also applied to reproduce the

structure and flexibility of the nanotubes. Two kinds of angles, corresponding to those highlighted in Fig. 5a, were restrained by potentials of the following form:

$$V_{a,i} = \frac{k_{a,i}}{2}\left(\cos\theta_i - \cos\theta_{0,i}\right)^2 \tag{2}$$

Where i indexes the angle type (1 or 2), and $k_{a,i}$ and $\theta_{0,i}$ are the force coefficient and equilibrium value associated with the i-th angle.

Non-neighboring CG-beads interact with each other utilizing Lennard-Jones potentials that implement the steric hindrance, mutual attraction, and hydrophobic effects driving the interaction between the CONTs. The term has the form:

$$V_{LJ} = 4\varepsilon\left(\left(\frac{\sigma}{r}\right)^{12} - \left(\frac{\sigma}{r}\right)^{6}\right) \tag{3}$$

Where ε is the energetic scale of the potential and σ is the length scale. We distinguish two kinds of non-bonded interactions described by Eq. (3), those between beads belonging to different CONTs, with parameters ε, σ, that regulate the interaction between the tubes, and those between beads belonging to the same CONT, with parameters ε', σ', that regulate the self-interactions within the tube. In all the CG models, the Lennard-Jones potential was truncated and shifted to 0 at a distance of $r_{cut} = 3.54$ nm.

The solvent is represented implicitly via the noise term in Langevin dynamics and the interaction between the assembly beads, which also encode the solvophilic/phobic behavior of the nanotubes. As outlined in the main text, the different parameters of the potential terms in Eqs. 1-3 was tuned to reproduce the behavior of the AA model in DCM solvent. First, we tuned the bonded potential CG parameters (Eqs. 1 and 2) by comparing the AA-MD of a single, equilibrated 16-layer-CONT with that of an equally sized CG-CONT in order to tune the interactions of a single tube in solution. The length of these CG-MD runs was of 10^7 integration steps (τ).

To this end, we compared the AA and CG distributions of the bond distance and angles obtained and set the force constants and equilibrium values accordingly. In Supplementary Figure 39, we report the comparison of the distributions obtained with AA-MD and CG-MD with the selected parametrization values, reported in Table S1. It is worth noting that in the chosen parametrization, the potential acting on angle 2 is inactive ($k_{a,2} = 0$), because angle 1 potential, together with the intra-tube excluded volume interactions, already enforce the distribution of angle 2 to a satisfactory agreement with the AA one. Due to the vast difference in resolution between the AA and CG descriptions, we looked for the best possible qualitative agreement, as the fine details of the CONT geometry, accessible with the AA description, are necessarily out-of-reach with the minimalistic CG model. In this phase, we also set the parameters ε' and σ', reported in Table S1. For monitoring and tuning the angular and bond distributions of the beads, we have used the analysis tools available in the *Swarm-CG* software developed by our group.[20]

After parametrizing the model of a single tube in solution, we proceeded in tuning the parameters of the non-bond interaction between the CG beads belonging to different CONTs, namely ε and σ (respectively, depth and position of the Lennard-Jones, LJ, minimum which dictates the bead-bead non-bond interaction strength). As explained in the main text, for this purpose, we performed umbrella sampling calculations, mirroring the procedure employed to obtain the free energy of lateral binding of two CONTs via the AA model (further details in the following). We repeated

the umbrella sampling calculations systematically varying the ε values in the range between 1 and 6 kJ mol^{-1}. The length scale σ was instead maintained at the fixed value of $1.51\ nm$, in order to avoid inter-penetration of the interacting CONTs. All parameters used in the CG model are reported in Table S1.

V_b(Eq. 1)		$V_{a,i}$(Eq. 2)				V_{LJ}(Eq. 3)			
k_b [kJmol^{-1}nm^{-2}]	r_0 [nm]	$k_{a,1}$ [kJmol^{-1}]	$\theta_{0,1}$ [°]	$k_{a,2}$ [kJmol^{-1}]	$\theta_{0,2}$ [°]	σ [nm]	ϵ [kJmol^{-1}]	σ' [nm]	ϵ' [kJmol^{-1}]
967.2	1.74	10.0	106.1	0	45.3	1.51	1.0-6.0	1.25	0.2

Supplementary Table 2: Parameters of CONT-1 CG model.

An example of the interwining phenomenon observed in water with the CG models developed herein is available as CG_model_intertwining.mp4.
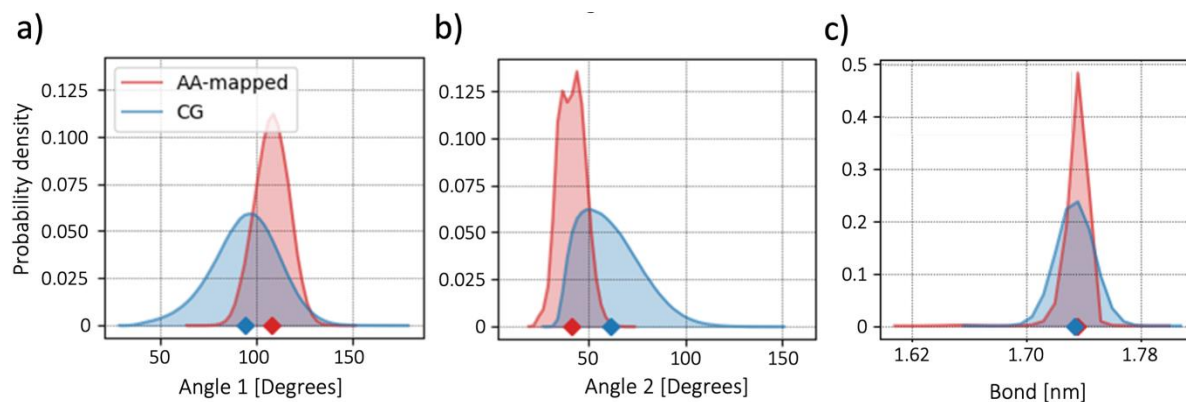

Supplementary Figure 39: Angles and bond distribution obtained from CONT-1 AA- and CG-MD simulations. a) Distribution of angle 1 formed by the centers of mass of neighboring TAT moieties (red curve) and by the corresponding beads in the CG model (blue curve). b) Distribution of angle 2 formed by the centers of mass of neighboring TAT moieties (red curve) and by the corresponding beads in the CG model (blue curve). Angles 1 and 2 are shown in Fig. 4a in the main text. (c) Distribution of the CG bond, namely the distance between the centers of mass of neighboring TAT moieties (red curve) and between the corresponding beads in the CG model (blue curve).

We also performed the simulation of two long (500 TAT ring layers, corresponding to a tubule length of ~850 nm of length) CONTs interacting with variable strength ε. Initial configurations containing two parallel tubes at a distance of 6.4 nm between each other were generated. After preliminary minimization via steepest-descent and short equilibration cycles with a 0.1τ integration step, each of these systems simulated for 10^8 steps of CG-MD simulation conducted in periodic boundary NVT (constant N: number of particles, V: box volume, and T: temperature during the run) conditions. All CG-MD simulations used a leapfrog stochastic dynamics integrator, with an inverse friction constant of $\tau_t = 25\tau$, regulating the solvent viscosity and thermalization of the system at $T = 20\ °C$.

The umbrella sampling calculations to compare the tube-tube lateral interactions with the AA case were conducted mirroring the AA model's procedure. In particular, two CONT CG portions composed of 6 TAT ring layers each (same length of the AA analysis) were placed in a parallel configuration and maintained at a fixed distance via harmonic potential restraining the distance between the two centers of masses of the tubes. This was repeated for 40 runs, each with a different equilibrium distance between the tubes, ranging from 2.86 nm to 9.0 nm. Also, in this case, the CG tubules portions were allowed to approach each other only in parallel fashion and were prevented from rotating by using restraining potentials restraining the centers of mass of both ends within a cylinder of 2.89 nm. The force constant of the harmonic potential restraining the distance between the tubes was $967.2\,\mathrm{kJ\,mol^{-1}nm^{-2}}$. The resulting trajectories were then combined using the weighted histogram analysis method to obtain the potential-of-mean-force profiles. We extracted the lateral interaction free-energies reported in Supplementary Figure 38c.

Structure and parameter files for the AA and CG models of the CONT-1 tubules used in the simulations are available at https://github.com/GMPavanLab/CONT/.
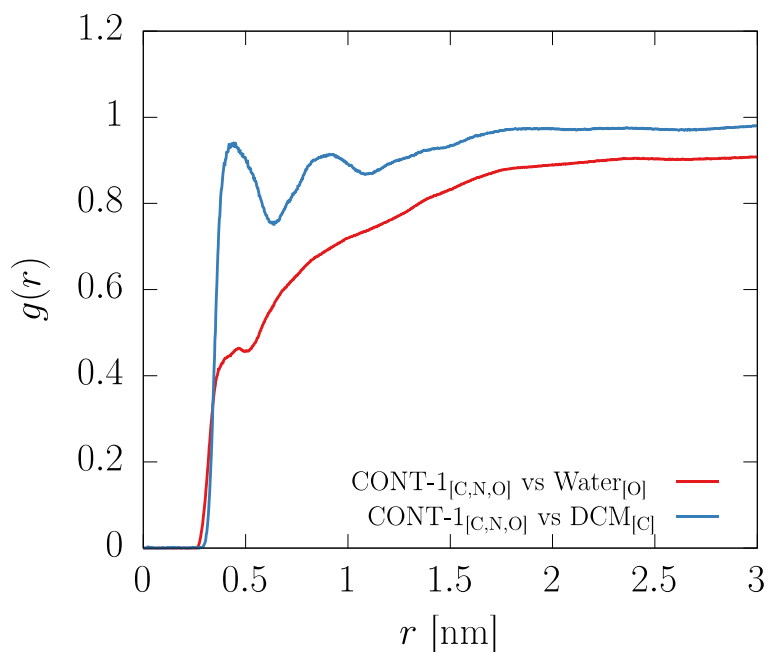
Supplementary Figure 40: Radial distribution *g(r)* of the AA CONT-1 model equilibrated MD in water (red) and DCM (blue) solvents. The *g(r)* is computed using the distances between the heavy atoms of the CONT-1 (C, N, O) and the Oxygens of the water molecules or the Carbons of the DCM molecules. See also Supplementary Movies 4 and 5 (zoomed view into the dynamics of solvent molecules close to the CONT-1 surface in DCM and water respectively).
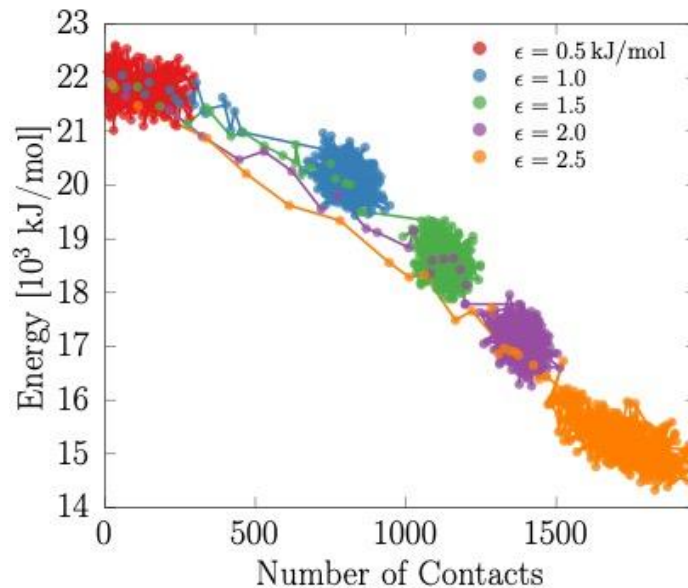
Supplementary Figure 41: Potential energy of two CONT-1 CG-models interacting with different values of ε, plotted as a function of the number of contacts among the CG-beads of the two tubes. The solid lines connect subsequent points along the CG-MD trajectory (25×10^6 steps are shown).

26.3 Coarse-Grained Interaction Energy Analysis

We calculated the CONT-CONT interaction energy, and decomposed it to electrostatic and van der Waals components in AA (because we underline the fact that our CG models treat in an implicit way electrostatic interactions). In particular, we considered the most-favorable bound configurations from the umbrella sampling calculations in the various solvents (Supplementary Fig. 39).

We have then computed the potential energy related to the CONT-CONT binding (ΔE) and we subsequently broken-down the latter in terms of electrostatic and van der Waals interactions (ΔE_{ele} and ΔE_{vdw} respectively). We found that the electrostatic component of the tubule-tubule interaction contributes less than the vdW component (the ΔE_{ele} contributing for ∼5-10% to the global CONT-CONT interaction). As expected, the total CONT-CONT ΔE becomes more and more favorable while the tubules are immersed in more polar solvents. For example, in DCM and THF the total ΔE between the CONTs is respectively ∼-44 and ∼-69 kJ/mol/layer, and globally weaker than in water (∼-114 kJ/mol/layer). The ΔE_{ele} components are ∼-14 and ∼-39 kJ/mol/layer in DCM and THF (equal to ∼6% and ∼9% of the total ΔE respectively), and ∼-46 kJ/mol/layer in water (∼7% of the total ΔE in this case). The ΔE_{vdw} components account for the (larger) remaining part of the ΔE, and account for ∼90-94% of the CONT-CONT interaction energy.

Overall, the trend seen in these interaction terms is qualitatively consistent with the one seen for the free-energy data obtained with the US calculations of Supplementary Figure 38. The fact that all components (ΔE_{ele} and ΔE_{vdw}) of the CONT-CONT interaction (ΔE) increases/reduces in similar way when going from one solvent to another suggests that in these cases the CONT-CONT interaction is mostly controlled by solvent effects rather than by some specific interactions between

CONT groups that may become more/less relevant in the different environment (basically, the CONTs assemble together more/less strongly as a global/average effect of their affinity/solubility for/in the solvent).

26.4 Preparation and video editing for Supplemental Movies

The video Supplementary Movie 1 and Supplementary Movie 2 uploaded as supplementary materials are related to the molecular dynamics of 16 TAT layers, running for 10 ns long in DCM and water, respectively. The structure of the assembly is sampled every 40ps, while running on a 2fs timestep. The dynamics reported in the video is then averaged over 5 frames in order to make the video smooth and understandable. The CONT assembly is represented without showing the H-atoms in licorice. The videos Suplementary Movie 4 and Supplementary Movie 5 are related to a 1ns-long MD simulation taken from the same system as before. In order to increase the understanding of the solvent dynamics within the first solvation shells, we make a zoom of on the previous structure and we highlight with different colors the solvent molecules that are within 3nm of the solute. Here the snapshots are sampled every 2 ps, and the dynamics is averaged over 2 frames in order to reduce the noise. The example related to the intertwining of the CG models of CONT fibers uploaded as Supplementary Movie 3, is related to $5 \cdot 10^7$ steps of CG-MD with ε=2.0. The system here is sampled every $5 \cdot 10^4$ steps, and the dynamics is smoothed over a window of five frames.

VMD was used to render each snapshot of the dynamics.[21] The final encoding of the video-files was done using ffmpeg.[22]

Section 27: Reference

1. White N. G., MacLachlan, M. J. Soluble Tetraaminotriptycene Precursors. *J. Org. Chem.* **80**, 8390–8397 (2015).
2. Sun, Q. et al. Pore Environment Control and Enhanced Performance of Enzymes Infiltrated in Covalent Organic Frameworks. *J. Am. Chem. Soc.* **140**, 984–992 (2018).
3. Xu, H., Gao, J., Jiang, D. Stable, crystalline, porous, covalent organic frameworks as a platform for chiral organocatalysts. *Nat. Chem.* **7**, 905–912 (2015).
4. Berendsen, H. J. C., van der Spoel, D., van Drunen, R. GROMACS: A message-passing parallel molecular dynamics implementation. *Comput. Phys. Commun.* **91**, 43–56 (1995).
5. Abraham, M. J. et al. GROMACS: High performance molecular simulations through multi-level parallelism from laptops to supercomputers. *SoftwareX* **1**, 19–25 (2015).
6. Tribello, G. A., Bonomi, M., Branduardi, D., Camilloni, C., Bussi, G. PLUMED 2: New feathers for an old bird. *Comput. Phys. Commun.* **185**, 604–613 (2014).
7. The PLUMED Consortium, Promoting transparency and reproducibility in enhanced molecular simulations. *Nat. Methods.* **16**, 670–673 (2019).
8. Wang, J., Wolf, R. M., Caldwell, J. W., Kollman, P. A., Case, D. A. Development and testing of a general amber force field. *J. Comput. Chem.* **25**, 1157–1174 (2004).

9. Wang, J., Wang, W., Kollman, P. A., Case, D. A. Automatic atom type and bond type perception in molecular mechanical calculations. *J. Mol. Graph. Model.* **25**, 247–260 (2006).

10. Bayly, C. I., Cieplak, P., Cornell, W., Kollman, P. A. A well-behaved electrostatic potential based method using charge restraints for deriving atomic charges: the RESP model. *J. Phys. Chem.* **97**, 10269–10280 (1993).

11. Frisch, M. J. et al. 2016. Gaussian Inc. Wallingford CT.

12. Bussi, G., Donadio, D., Parrinello, M. Canonical sampling through velocity rescaling. *J. Chem. Phys.* **126**, 014101 (2007).

13. Berendsen, H. J. C., Postma, J. P. M., DiNola, A., Haak, J. R. Molecular dynamics with coupling to an external bath. *J. Chem. Phys.* **81**, 3684–3690 (1984).

14. Bochicchio, D., Salvalaglio, M., Pavan, G. M. Into the dynamics of a supramolecular polymer at submolecular resolution. *Nat. Commun.* **8**, 147 (2017).

15. Shema-Mizrachi, M., Pavan, G. M., Levin, E., Danani, A., Lemcoff, N. G. Catalytic chameleon dendrimers. *J. Am. Chem. Soc.* **133**, 14359-14367 (2011).

16. Jorgensen, W. L., Chandrasekhar, J., Madura, J. D., Impey, R. W., Klein, M. L. Comparison of simple potential functions for simulating liquid water. *J. Chem. Phys.* **79**, 926–935 (1983).

17. Torrie, G. M., Valleau, J. P. Nonphysical sampling distributions in Monte Carlo free-energy estimation: Umbrella sampling. *Journal of Computational Physics* **23**, 187-199 (1977).

18. Kumar, S., Rosenberg, J. M., Bouzida, D., Swendsen, R. H., Kollman, P.A. THE weighted histogram analysis method for free-energy calculations on biomolecules. I. *The method. J. Comput. Chem.* **13**, 1011-1021 (1992).

19. Zhu, F., Hummer, G. Convergence and error estimation in free energy calculations using the weighted histogram analysis method. *J. Comput. Chem.* **33**, 453-465 (2012).

20. Empereur-Mot, C. et al. Swarm-CG: Automatic Parametrization of Bonded Terms in MARTINI-Based Coarse-Grained Models of Simple to Complex Molecules via Fuzzy Self-Tuning Particle Swarm Optimization. *ACS Omega* **5**, 32823–32843 (2020).

21. Humphrey, W., Dalke, A. and Schulten, K., "VMD - Visual Molecular Dynamics", *J. Molec. Graphics,* **14**, 33-38 (1996).

22. FFmpeg Developers, "ffmpeg (Version 4.4)" [Software], 2016. Available from http://ffmpeg.org/